Mechanical compaction mechanisms in the input sediments of the Sumatra Subduction Complex- insights from microstructural analysis of cores from IODP Expedition- 362

Sivaji Lahiri[1]*, Kitty L. Milliken[2], Peter Vrolijk[3], Guillaume Desbois[1], Janos L. Urai[1]

[1]Institute of Tectonics and Geodynamics, RWTH Aachen University, Germany, Lochnerstrasse 4–20, 52056, Aachen, Germany

[2]Bureau of Economic Geology, The University of Texas at Austin, Austin, TX, 10611, USA

[3]Department of Earth and Environmental Science, New Mexico Institute of Mining and Technology, 801 Leroy Place, Socorro, NM 87801, USA

* Corresponding author: sivaji.lahiri2@gmail.com

Abstract

The input sediments of the North Sumatra subduction zone margin, drilled during IODP Expedition 362, exhibit remarkable uniformity in composition and grain size over the entire thickness of the rapidly deposited Nicobar Fan succession (seafloor to 1500 mbsf), providing a unique opportunity to study the micromechanisms of compaction. Samples were prepared from dried core samples from sites (U1480 and U1481) by both Ar-ion cross-section polishing and broad-ion beam cutting and imaged with a field-emission Scanning Electron Microscope (SEM). The shallowest samples (seafloor to 28mbsf) display a sharp reduction in porosity from 80% to 52% due to collapse of large clay-domain/matrix pores associated with rotation and realignment of clay-platelets parallel to the bedding plane. The deeper succession (28mbsf to 1500mbsf) exhibits less rapid reduction in porosity from 52% to 30% by the progressive collapse of silt-adjacent larger pores through bending and subsequent sliding/fracturing of clay particles. In addition, there is a correlated loss of porosity in the pores too small to be resolved by SEM.

Clastic particles show no evidence of deformation or fracturing with increasing compaction. In the phyllosilicates, there is no evidence for pressure solution or recrystallization: thus, compaction proceeds by micromechanical processes. Increase in effective stress up to 18 MPa (~1500mbsf) causes the development of a weakly aligned phyllosilicate fabric mainly defined by illite clay particles and mica grains, while the roundness of interparticle pores decreases as the pores become more elongated. We propose that bending of the phyllosilicates by intra-particle slip may be the rate-controlling mechanism.

30 Pore size distributions show that all pores within the compactional force chain deform, irrespective of size, with

31 increasing compactional strain. This arises because the force chain driving pore collapse is localized primarily

32 within the volumetrically dominant and weaker clay-rich domains; pores associated with packing around isolated

33 silt particles enter into the force chain asynchronously and do not contribute preferentially to pore loss over the

34 depth range studied.

Introduction

36 Muds are fine-grained sediments (>50% of particles <63μm diameter) comprising platy detrital clay minerals and

37 equidimensional detrital grains such as quartz, feldspar, calcite, etc. (Nakano, 1967; Hesse, R., 1975; Sintubin,

38 1994). Understanding the mechanical, chemical, and microstructural properties of mud and mudstone is of great

39 interest for rock property prediction in basic earth science, in exploration, subsurface integrity studies and

40 geotechnical engineering (Yagiz, S., 2001; Aplin and Macquaker, 2011; Lazar et al., 2015). The chemical and

41 physical behavior of marine muds plays a critical role in defining the geometry of accretionary prisms, locating

42 the décollement for fault rupture (Vrolijk, 1990; Chester et al., 2013) and understanding subduction zone

43 earthquakes and tsunamis (Dean et al., 2010; Chester et al., 2013; Hüpers et al., 2017).

44 Marine mud is deposited with a highly porous isotropic fabric (Bowles, 1969; Bennett et al. 1981; 1991);

45 depositional porosity in mud is about twice as high as in sand (e.g., Velde, 1996, Lundegard, 1992). In contrast,

46 mudstones have low porosities, modal pore sizes measured in nm, and an absence of textural controls on porosity

47 (e.g. Aplin et al., 2006; Milliken et al., 2012; 2013). The processes in this dramatic evolution of porosity have

48 similarities to compaction of sand to sandstone, comprising a combination of compaction and cementation

49 (Milliken and Day-Stirrat, 2013), although the much smaller, elongated phyllosilicate grains increase the role of

50 clay-bound water in the process (Karaborni et al., 1996). Whereas a refined and somewhat predictive

51 understanding exists for porosity evolution in sand and sandstones (e.g., Lander and Walderhaug, 1999; Paxton et

52 al., 2002; Lander et al., 2008; Ajdukiewicz and Lander, 2010, Desbois et al., 2011), such a model is at best

53 preliminary for muds and mudstones (Pommer and Milliken, 2015; Milliken and Olson, 2017). It seems clear that

54 the composition of the grain assemblage importantly sets the stage for porosity evolution in muds (Milliken, 2014),

55 cementation being the greatest in muds with abundant biogenic debris. In contrast to sandstones, however,

56 cementation is far less common globally in mudstones (Milliken, 2019), leading to the notion that mechanical

57 compaction may be far more important in muds. In addition, depositional environment also strongly controls

58 porosity evolution, compaction and diagenesis in mudrocks (e.g. Burland, 1990; Baruch et al., 2015; Delle Piane

59 et al., 2015) as the initial clay and rigid grain compositions significantly affect both compaction (as this manuscript

60 shows) and subsequent diagenetic alteration due to variations in composition. Establishing the expected

61 compaction behavior for muds in a setting of well-constrained mud properties is an essential contribution that our

62 study hopes to serve.

63 Investigations of mud and mudstone compaction are usually based on proxy data, such as velocity or density,

64 rather than direct measurements of porosity (e.g., references in Mondol et al., 2007). Direct measurement of

65 porosity is broadly classified into two categories: 1) experimental compaction in the laboratory; (e.g., Mitchell,

66 1956; Bennett et al. 1981; Griffiths and Joshi, 1989; 1990; Vasseur et al. 1995; Mondol et al. 2007; Fawad et al.

67 2010; Emmanuel and Day-Stirrat, 2012), and 2) studies on natural samples those are compacted in situ with depth
68 (e.g., Meade, 1964; Ho et al., 1999; Aplin et al. 2003; 2006; Day-Stirrat et al., 2008; 2010; 2012; Milliken et al,
69 2012; 2013). A common shortcoming of the studies on the naturally compacted samples is the assumption that the
70 bulk porosity is a direct measure of compaction although porosity loss has contributions of both compaction and
71 cementation (Ehrenberg, 1989; Lundegard, 1992; Paxton et al., 2002), and this can only be accomplished by
72 petrographic inspection (Milliken and Curtis, 2016). Experimental studies generally avoid this shortcoming as the
73 sample sets generally do not undergo any chemical change during the investigation. Studies of shallowly buried
74 units (like the present study) are the ones most likely to avoid the complication of cementation, especially if
75 temperatures are low and bulk grain assemblages are siliciclastic (Milliken, 2008, 2014).

76 Previous studies report contrasting ideas about the mechanisms of mechanical compaction of mud. Some studies
77 conclude that rotation is the dominant particle scale mechanism for mechanical compaction (Bowles et al., 1969;
78 Oertel and Curtis, 1972; Vasseur et al., 1995), although other particle scale-deformation mechanisms were not
79 investigated by these authors. A few studies state that burial compaction significantly increases the alignment of
80 phyllosilicate (clay and mica) parallel to the bedding planes (Bowles et al., 1969; Oertel and Curtis, 1972; Vasseur
81 et al., 1995) (a detailed review of the previous studies on mechanical compaction is given in Document S1 in
82 Supplementary data). Other studies suggest that intense mechanical compaction (i.e. effective stress) has a limited
83 impact on the development of phyllosilicate fabric in mud (Ho et al., 1999; Aplin et al., 2006; Day-Stirrat et al.,
84 2008; 2011). In addition, earlier authors concluded that an increase in effective stress causes preferential loss of
85 larger pores, and as a result, the mean porosity of the samples decreases (Delage and Lefebvre, 1984; Griffiths and
86 Joshi, 1989; 1990; Emmanuel and Day-Stirrat, 2012). With increasing consolidation stress, a bimodal pore size
87 distribution curve shifts toward smaller pore sizes as larger pores rapidly collapse (Griffiths and Joshi, 1989; 1990;
88 1991). These studies investigated the changes in particle alignment and reduction in porosity (Ho et al., 1999;
89 Aplin et al., 2006; Day-Stirrat et al., 2008; 2011) but without imaging the evolution of pore morphology with
90 increasing compactional strain. Moreover, in previous studies, the authors mainly performed laboratory
91 consolidation experiments on lab produced particle packs, and used conventional techniques, such as mercury
92 intrusion porosimetry and high-resolution X-Ray pole figure goniometry (HRXTG) to understand the evolution of
93 pore size distribution with consolidation stress (Ho et al., 1999; Aplin et al., 2006). Studies on naturally compacted
94 samples are less common.

95 We received 55 mud samples from drill cores collected during IODP Expedition 362 west of the North Sumatra
96 subduction zone margin and investigated the evolution of petrographic microstructure and pore morphology as a
97 function of compactional strain. Apart from general implications for global mudrocks, we hope this investigation
98 will also contribute to studies that seek to predict rock properties in the deeper subsurface at the Sumatra
99 subduction front.

100

Geological background and drilling

The Sumatra subduction zone extends 5000km from the Andaman-Nicobar Islands in the northwest to the Java-Banda arc in the Southeast (Fig.1a and b) (Prawirodirdjo et al., 1997; Hippchen and Hyndman, 2008). The trench of the Sumatra subduction zone (Fig.1a) developed on the subducting Indo-Australian Plate at a convergence rate of 5.5 cm/yr in the north and 7.23 cm/yr in the South (Ghosal et al., 2014; Moeremans, and Singh, 2015).

On 26th December 2004, the west coast of Northern Sumatra recorded one of the largest earthquakes (Mw-9.3) in the 21st century, generating a devastating tsunami in the Indian Ocean (Ammon et al., 2005; Lay et al., 2005). Understanding the mechanism(s) behind this unprecedented event was the central idea behind IODP Expedition 362 (Fig.1). The main objective of the expedition was to collect core and log data from the incoming sedimentary succession of the Indo-Australian oceanic plate to understand the seismogenic process related to the margin (Dugan et al., 2017; McNeill et al., 2017a). During the expedition in 2016, drilling was performed on two sites: U1480 (Holes E, F, G and H) and U1481 (Hole A) located on the oceanic plate west of the North Sumatra subduction margin and east of the Ninety East Ridge (Fig.1a, b) (Dugan et al., 2017). The drilling sites recovered a complete, 1.5 km thick sedimentary section from late Cretaceous to Pleistocene down to the basement of basaltic crust (Dugan et al., 2017; McNeill et al., 2017a).

The input sedimentary section of the Sumatra subduction zone comprises the distal part of the trench wedge, Nicobar fan sequence, and pre-fan pelagic section on the basaltic crust at the bottom (Dugan et al., 2017; McNeill et al., 2017a). At Site U1480, the entire recovered section was categorized into six lithological entities, Units I to VI (Fig. 1c) (McNeill et al., 2017a). Unit I (0 to 26.72 mbsf) consist of unconsolidated calcareous clay, silty clay with alternating fine sand (McNeill et al., 2017a). Unit II from 26.72 to 1250 mbsf consists of three subunits (IIA, IIB and IIC) and mainly exhibits alternating fine-grained sand and silty clay to silt (McNeill et al., 2017a). Unit III (1250 ~ 1327 mbsf) is divided into two subunits: Unit IIIA and IIIB (McNeill et al., 2017a). Unit IIIA consist of thin to medium-bedded, gray-green or brown mudstone and intercalated siltstone, and Unit IIIB is composed of reddish-brown tuffaceous silty claystone with fragmented sponge spicules and radiolaria (McNeill et al., 2017a). The boundary between Units IIIA and IIIB (1310 mbsf) at this site marks the base of the Nicobar Fan and the beginning of the thin pre-fan succession (Pickering et al., 2020). Units IV, V, and VI include volcanoclastic rocks with tuffaceous sandstone, conglomerates, and basaltic oceanic crust, respectively. At Site U1481, the pre-fan succession was not encountered and a Unit III, a thicker equivalent of Subunit IIIA at Site U1480, represents the material of the lower Nicobar Fan (see Figure F15, in Site U1481 report; McNeil et al., 2017a). This study is restricted to the thin, distal trench wedge (Unit I) and Nicobar fan sequence (Units II and IIIA, which is equivalent to Unit-III at U1481).

X-ray diffraction (XRD) of bulk samples and clay fractions at Site U1480 show a clay mineral assemblage dominated by illite with lesser amounts of smectite and chlorite (Rosenberger et al., 2020) (Fig.2a, b, c, and d; Table S1 and Figure S1 in Supplementary data). Clay mineral data arise from three separate analyses: (1) bulk sample analyses of air-dried samples (random orientation) onboard ship used to define the proportion of all clay minerals in a sediment sample (McNeill et al., 2017a), (2) air-dried clay-sized samples (sedimented and oriented) analyzed in New Mexico that define the types and abundances of clay minerals (Rosenberger et al., 2020; note

that abundances limited to clay minerals used in the reference mixtures, which include discrete illite and discrete smectite), and (3) glycol-saturated clay-sized samples (sedimented and oriented) analyzed in New Mexico that determine the amount of illite in mixed-layer I/S, defined as smectite in #2 (Rosenberger et al., 2020). Note that the amount of illite in mixed-layer I/S is only accounted for in the expandability value and never in the discrete illite value.

Siliciclastic samples consist of 50-70% clay minerals (McNeill et al., 2017a). Smectite fraction, determined from the air-dried, clay-sized samples (as described in Underwood et al., 2020) is more abundant in Unit I than Unit II, where smectite abundance ranges from 5-30% with rare samples containing as much as 45% smectite. In Unit II, smectite fraction ranges from 10-30% with local discreet enrichments as great as 40-45%. Smectite again increases in Unit III, reaching a value as high as 68% in the samples attributed to the Nicobar Fan section. There is a weak increase in the expandability of mixed-layer I/S with depth (determined from glycol-saturated, clay-sized samples; Rosenberger et al., 2020; Underwood et al., 2020; Figure-S2 in Supplementary data), suggesting a shift in clay mieral provenance rather than smectite-illite diagenesis. Montmorillonite is interpreted as the smectite mineral (Rosenberger et al., 2020). Chlorite + kaolinite abundance is similar in Units I and II, ranging from 8 to 20% with rare occurrences as high as 24%; Unit III is almost devoid of chlorite + kaolinite. Heating experiments on select samples indicate that chlorite makes up 66-100% of this mineral category (Rosenberger et al., 2020). Illite comprises the remainder of the clay mineral assemblage, ranging from 50-79% in Unit II while Unit I is correspondingly less illite-rich (42-70%). In the Unit III Nicobar Fan section, illite makes up only 18-36% of the clay fraction. Again, it should be noted that, the shipboard methodology used for XRD analysis is semiquantitative and has limitations in identifying bulk mineralogy of the samples; the abundance of mixed-layer clays and the expandability of mixed-layer I/S is only inferred qualitatively (McNeil et al. 2017a; Underwood et al., 2020).

The Nicobar fan sequence exhibits almost compositionally homogeneous (silt/clay ratio; mostly 'silty-clay') subunits with uniform grain size (McNeill et al., 2017a), and a history of rapid deposition (125-290 m/my; Backman et al., 2019). The sedimentary sequence exhibits no evidence of uplift and currently occurs at maximum burial depth. The drilling sites are 255 km away from the deformation front; thus, the samples are undisturbed by tectonic faulting associated with subduction (Fig.1b). In addition, owing to the scarcity of biogenic grains and the low temperatures encountered (<68°C), cementation is only observed as highly localized concretions (Red colored symbols in Fig.2e, f, g, and h) (McNeil et al., 2017b; Torres et al., 2022). Such a homogeneous sedimentary succession extending across 1.5 km depth is rare in sedimentary basins. Hence, these samples provide us with a unique opportunity to study depth-wise variation in microstructure as a function of vertical effective stress with few complications from multiple causes of porosity loss.

Sampling and Methods

This study is based on two sample sets that were obtained from Sites 1480 (Holes E, F, G, and H) and 1481 (Hole A) independently and analyzed by slightly different methods. Samples have been prepared using Ar-ion cross-section polishing and analyzed using a scanning electron microscope equipped with a field emission gun (BIB-SE technique). The first sample set (33 mud samples; depth 1.24 to 1300 mbsf) was prepared and analyzed at RWTH Aachen University, Germany. The second sample set (22 samples; depths 6.25 to 1493.30 mbsf) was prepared and

175 studied at the Bureau of Economic Geology (BEG) at the University of Texas at Austin. Respective core
176 description of these 55 mud samples and their bulk mineralogy data are tabulated in Table-1.

BIB-SEM technique (First set of samples, Aachen University)

Sample preparation for BIB-SEM and imaging

179 After drilling, the samples were stored at Kochi drill core repository (IODP), Japan for four years (2016 ~ 2020)
180 in refrigerated storage areas, maintaining a temperature of ca. 4°C and 80% humidity (http://www.kochi-
181 core.jp/en/iodp-curation/curation-sop_2.html). We received a total of 33 freeze-dried mud samples (SN-1 to SN-
182 33 in Table-1) for analysis at Aachen. The samples were collected using a tube inserted perpendicular to the cut
183 face of the drill core in such a way that the notch of the tube identified the top of the sample so the orientation of
184 bedding planes for each sample was known. In Fig. 1d, a tube sample received from the IODP repository is shown,
185 where the red line on the top of the tube identifies the notch. Subsamples (10 x 5 x 2 mm^3) were cut from the
186 individual freeze-dried samples using a razor blade. These subsamples were pre-polished using silicon carbide
187 (SiC) paper to reduce the roughness of the surface down to 10 μm. Further, Broad Ion Beam (BIB) polishing was
188 carried out using a JEOL SM-09010 cross-section polisher for 10 hours at 6 kV and 150 μA. BIB reduces surface
189 damage by removing a 100 μm thick layer to generate a high-quality polished cross-section of 1-2 mm^2 with a
190 topography less than 5 nm (Desbois et al., 2009).

191 After polishing, the BIB cross-sections were coated with tungsten and imaged with a Zeiss Supra 55 SEM with
192 SE2, BSE, and EDX detector (Figure S3 in Supplementary data). SE2 images were used to image porosity and
193 BSE images are combined with an EDX map as well as EDX point analysis for identifying mineral phases. For
194 each cross-section, we made mosaics of hundreds of SE2 and BSE images at a magnification of 20,000x (~14.3
195 nm pixel value) and 10,000x respectively, with an overlap of 20% to 30%, (Klaver et al., 2012; 2015; 2016; Hemes
196 et al., 2013; 2015; 2016; Laurich et al., 2014). The mosaics are stitched together using Aztec software preserving
197 the original pixel resolution. Finally, these stitched images are used for the segmentation of pore spaces, minerals,
198 and other respective analyses.

Image segmentation and pore analysis

200 For quantifying porosity and pore morphology, individual SE2 image mosaics were segmented using a 'seed and
201 grow' algorithm (Adams and Bischof, 1994) implemented with a MatLab code (Jiang et al., 2015; Schmatz et al.,
202 2017) (Figure S3 in Supplementary data). The 'seed and grow' algorithm works based on the difference in intensity
203 of greyscale value in an image (bright = minerals, dark= pores). After automatic segmentation, individual pores in
204 SE2 images are manually corrected if required.

205 Similarly, using ImageJ software (threshold toolbox and machine learning algorithm), segmentation of the
206 individual mineral phases was carried out combining BSE images and EDX elemental maps. While quartz, calcite,
207 pyrite, mica minerals are efficiently segmented using these tools, feldspars are found difficult to segment because
208 of similar composition as clay (Figure S4, S5 and S6 in Supplementary data). Finally, corrected pore segmented

209   SE2 mosaics are overlaid on the phase maps using the 'georeference' tool of QGIS (http://qgis.osgeo.org), (Figure

210   S4, S5 and S6 in Supplementary data).

Pore detection resolution (PPR) and representative area analysis (REA)

212   'Practical pore detection resolution' (PPR) indicates the pore sizes above which one can assume to detect 100% of

213   the pores present in the SE2 mosaic (Klaver et al., 2012). In agreement with earlier results using this instrument

214   (Klaver et al., 2012; 2015; 2016; Hemes et al., 2013; 2015; 2016; Laurich et al., 2014), we found PPR of ~2000

215   nm^2 and ~8500 nm^2 for the magnification of 20,000x and 10,000x images, respectively, corresponding to 10 pixels.

216   After segmenting all minerals, representative elementary area analysis (REA) was performed using the box

217   counting technique on mineralogical phase maps (Kameda et al., 2006; Klaver et al., 2012). Similar steps are also

218   followed for determining a representative elementary area for SE2 images. The estimated REA values using SE2

219   and BSE mosaics for the analyzed 33 mudstone samples are documented in Table S2 in Supplementary data.

220   Porosity, pore morphology, pore size, and the statistical distribution of pores were obtained using image analysis

221   techniques on 2D images collected using BIB-SEM technique. Because pores are non-spherical 3D objects that

222   are cut perpendicular to the bedding plane to acquire a 2D image dataset, there may be random and systematic

223   errors when comparing 2D and 3D results. We plotted shipboard measured MAD (moisture and density) porosity

224   vs depth (Fig.2e) and also BIB-SEM porosity vs depth for the analyzed samples (Fig.3a), where MAD porosity

225   documents bulk porosity for the sample, and BIB-SEM porosity represents 2D cuts of the non-spherical 3D

226   pores/porosity. As there is a first-order correspondence between the two porosity measurements, we deduce that

227   porosity and pore size distributions obtained from 2D image analysis reflect the bulk rock porosity and 3D pore

228   size distribution of the samples. In addition, the estimated REA appears appropriate for minimizing systematic

229   errors in the bulk pore characteristics of the sample.

230

Ion polishing and SEM technique (second set of samples; BEG, UT Austin).

232   22 Samples (SN-34 to SN-55 in Table 1) were taken shipboard from the sample half of the still-wet core in small

233   plastic tubes (similar to the ones used for the sample set at Aachen) inserted into the core by manual pressure. The

234   tubes were removed from the core and sealed in plastic bags. In the laboratory at the BEG, sample bags were

235   opened, and the muds were allowed to dry slowly in the tubes over several weeks. No discernible shrinkage was

236   observed as the dried core pieces still fully filled the tubes. The tubes were carefully removed, and a small cube

237   (approximately 0.5 to 1 cm^3) was cut using a sharp knife and small hand saws; an orientation mark was placed on

238   the cube to indicate the bedding direction. Bed-perpendicular surfaces were prepared by Ar-ion cross-section

239   polishing, using the Leica EM TIC020 triple ion beam miller and coated with Ir for imaging. Manual placement

240   of the cut cubes into the ion mill is not precise so the ion-polished surfaces have slight variation from perpendicular

241   to bedding. Pore imaging was performed on the FEI Nova NanoSEM 430 using the in-lens SE detector, a 30 μm

242   aperture, 15 KeV accelerating current, a working distance of around 5–6 mm, and an intermediate-range sample

243   current (spot size = 3nm, mid-range for the instrument). Randomly selected views (typically 3-6) of all samples

244 were collected at 6000x machine magnification; additional views illustrating pore types and pore/grain
245 relationships were made at 10,000x to 30,000x (machine magnification).

246

Results

Compaction strain derived from MAD-porosity data

249 During Expedition 362, mass and volume of mud samples were measured in both wet and dry states using a high
250 precision electronic mass balance and helium pycnometer (http://www-odp.tamu.edu/publications/tnotes/tn37/
251 tn37_8.htm). Using the obtained mass and volume dataset for wet and dry conditions, bulk MAD (moisture and
252 density) porosities were calculated. Porosity values reported by McNeill et al. (2017b) and downloaded from IODP
253 databases serve as the basis for strain calculations.

254 Shipboard MAD porosity for mud samples exhibits a sharp reduction from 80% to 52% from the seafloor to 28
255 mbsf (Fig.2e). Deeper samples display a comparatively smaller reduction in porosity of approximately from 52%
256 to 30% over a depth range of 28 to 1500 mbsf (Fig.2e and f).

257 We calculated compaction strain following a method proposed by Nollet et al. (2005) and subsequently used by
258 Neagu et al. (2010) (Fig.2g and h), assuming 1D consolidation and no change in solid volume. The compaction
259 strain (ε_c) is then computed as:

260 $$\varepsilon_c = \frac{1-\phi_0}{1-\phi_1}$$ (Eqn-1)

261 Here ϕ_0 = initial porosity, and ϕ_1 = final porosity. Samples from sites U1480 and U1481 show no evidence of
262 tectonic faults (McNeill et al., 2017a), supporting an assumption of 1D strain. We considered the initial porosity
263 ϕ_0 as the MAD porosity at 0.6 mbsf depth (ϕ_0 = 80%). Compaction strain following Eqn-1 (Table S2 in
264 Supplementary data), is plotted against depth in Fig.2g and h. Compaction strain increases from 1 to 2.05 from the
265 seafloor to 28 mbsf (i.e. Unit I), and from 2.00 to 3.05 from 28mbsf to 1500 mbsf (Fig. 2g and h).

266 Another common measure of compaction is the intergranular volume (IGV; Paxton et al., 2002), which
267 corresponds to the sum of intergranular porosity and intergranular cement. In some mudstones, it may be necessary
268 to calculate IGV differently because of the presence of abundant primary intragranular pores and pore-filling
269 bitumen (Milliken and Olson, 2017). In our sample set, cement is absent, and IGV is taken to equal the bulk
270 porosity from shipboard MAD measurements.

271 Compactional porosity loss (COPL), referenced against the original sediment volume, is calculated from the initial
272 primary intergranular porosity (Pi; 80% in this case) and the IGV as follows (Ehrenberg, 1989, Lundegard, 1992;):

273 COPL= Pi-(((100-Pi) x IGV)/(100-IGV)) (Eqn-2)

274   At an IGV of 50%, COPL is 60%; in the deepest samples in the Nicobar fan (IGV of around 30%) COPL is 70%
275   (Table S2 in Supplementary data).

Description of grain microstructure and pore morphology

277   To have consistency in the data set, we prepared SE2 mosaics for all samples from the Aachen sample set at
278   20,000x magnification covering an average 100×100 μm^2 area. In addition, to examine the effect of magnification
279   on BIB-SEM porosity and representative area analysis (REA), three samples (i.e. SN-7, SN-15, and SN-29) were
280   also imaged each at 5,000x and 10,000x magnification, respectively. A decrease in magnification and resolution
281   reduces visible BIB-SEM porosity.

282   We observed consistent results for the REA analysis. For SE2 mosaics, REA varies between $45\times45\mu m^2$ to 85×85
283   μm^2 at 20,000x magnification, and for segmented phase maps, REA varies between 90×90 μm^2 to 130×130 μm^2
284   at 10,000x magnification. In the UT sample set, the standard images taken at 6000x with machine magnification
285   are $49.7x45.7$ μm^2, so these images are also within the estimated REA range.

286   Based on EDX elemental map or point analysis, six mineral phases occur in significant amounts in the Sumatra
287   samples: quartz, feldspar (K-feldspar, Na-feldspar), calcite, pyrite, micas (muscovite, biotite, and chlorite), and
288   clay. Based on XRD analyses (Rosenberger et al., 2020), the clay size fraction is dominated by illite. Clay + mica
289   percentage in these mudstone samples varies between 65% to 75%. Samples SN-1 (77%) and SN-4 (76%) have
290   more clay + mica, whereas SN-7, SN-9, SN-17, SN-28, SN-29, and SN-31 contain less clay + mica (<65%) (Table
291   S2 in Supplementary data). It should be noted that, using EDX analysis, we are able to differentiate Na-feldspar,
292   and K-feldspar considering the concentration of Na and K elements in the grains. However, the XRD dataset
293   provides only information about the overall percentage of plagioclase feldspar present in these samples (Table 1),
294   perhaps an artifact of different detection limits for EDX and XRD analyses.

295   Using BIB-SEM and automatic pore segmentation techniques, an average of >30,000 pores have been detected
296   for each individual sample in the Aachen sample set at 20,000x magnification. Correlating with the MAD data set,
297   the estimated BIB-SEM porosity reduces from 32% to 19% over a depth range of seafloor to 28 mbsf, while the
298   deeper samples display a smaller reduction from 19% to 10% over a depth range of 28 to 1500 mbsf respectively
299   (Fig.3a). Consistent with numerous previous studies, the results document a mismatch between bulk measured
300   porosity (MAD) and imaging porosity (BIB-SEM) (e.g., Hemes et al., 2013; Houben et al., 2014; Nole et al., 2016;
301   Oelker et al., 2019) (Table S2 in Supplementary data). We plotted BIB-SEM porosity vs MAD porosity and found
302   an approximately linear correlation with coefficient of determination ($R^2 = 0.8621$) (Fig. 3b). It should also be
303   noted that, although there is a correlation, there is a large difference in the porosity values which increases with
304   increasing porosity.

Type of pores

306   Intergranular pores contribute >99% of the total visible porosity. Intragranular pores (see below) are rare. The size
307   and shape of intergranular pores change during compaction (Table S3 in Supplementary data).

308   Intergranular pores are classified (Fig.4) based on the size of surrounding particles (irrespective of mineralogy):

309   1) Clay domain (matrix) pores, and 2) silt-adjacent pores. Based on the variation in size, clay domain pores are

310   divided further into: 1) Large clay domain pores (pore size $>5 \times 10^5$ nm^2) and the pore boundary is defined by more

311   than three clay particles; and 2) small clay domain pores (pore size $<5 \times 10^5$ nm^2) that occur between 2-3 clay

312   particles (see further details below). Large and small clay domain pores are classified by geometry as: 1) Elongate

313   pores (aspect ratio $>3:1$) and 2) equant-shaped pores (aspect ratio $<3:1$). Elongate pores consist of 1) Linear-

314   elongated pores, and 2) crescent-shaped elongated pores. Examples of different clay-domain pore types are shown

315   in Fig. 5, 6, and 7.

316   Silt-adjacent pores are categorized by two types: 1) large silt-adjacent pores are $>5 \times 10^5$ nm^2, and pore boundaries

317   are defined by more than three particles; and 2) small silt-adjacent pores include pore sizes $<5 \times 10^5$ nm^2, and pore

318   boundaries are defined by two/three particles (see further detail on the modal sizes of these pore types below).

319   Large and small silt-adjacent pores are either: 1) Equant shaped (aspect ratio $<3:1$) or 2) elongated (aspect ratio

320    $>3:1$). Further, elongated silt-adjacent pores consist of 1) linear-shaped elongated pores and 2) crescent-shaped

321   elongated pores. These pore types are highlighted in Fig. 5, 6, and 7.

Change in inter-particle pore morphology with depth

Seafloor to 28mbsf (Unit I)

324   The shallow mud samples in Unit I are unconsolidated and porous (Fig. 5a). We analyzed a total of 10 samples (6

325   samples at Aachen and 4 samples at UT Austin) from this depth range. Among them, two samples have been

326   analysed both in Aachen as well as in Austin, respectively. Sample SN-1 (1.24 mbsf) has a maximum MAD

327   porosity of 80%. We observe three types of clay particle contacts in the microstructure of SN-1; edge to edge (EE),

328   edge to face (EF), and face to face (FF) contacts (Table S4 in Supplementary data). Among them, EF and FF

329   contacts are abundant and EE contacts are rare. The sample exhibits abundant large clay domain pores and large

330   silt-adjacent pores that are equant with smooth edges and a rounded pore perimeter. The sample also contains

331   abundant linear-elongated and equant-shaped small clay-domain pores. Crescent-shaped small clay domain pores

332   are rare in the microstructure of this sample. Equant-shaped, small silt-adjacent pores are abundant. In addition,

333   linear elongated and crescent-shaped small, silt-adjacent pores are also common (Fig.5a; Table S3 in

334   Supplementary data).

335   With increasing compaction strain ($\varepsilon_c = 1.119$) and depth (5.1 mbsf; Figure S7 in Supplementary data), porosity

336   (MAD) reduces to 75% and corresponding COPL=19% (sample SN-2; Fig. 5b, Table S2 in Supplementary data).

337   The microstructures of SN-2 display are similar characteristics to those observed in sample SN-1, although there

338   are fewer large clay domain pores in SN-2 than SN-1. Linear elongated and equant-shaped small clay domain

339   pores are common Table S3 in Supplementary data), but crescent-shaped small clay domain pores are rare. The

340   microstructures of SN-2 exhibit abundant equant-shaped large and small silt-adjacent pores.

341   With an increase in compaction strain to $\varepsilon_c \sim 2.00$ (28 mbsf), the sample microstructure is dominated by FF contacts

342   (Fig. 5e), and EE and EF contacts are rare (Table S4 in Supplementary data). Additionally, large clay-domain

343   pores become infrequent in the microstructure (Fig.5e and Fig. 8). Crescent-shaped, small clay domain pores in

the microstructure are rare, whereas equant-shaped small clay domain pores are common. Both small and large silt-adjacent pores exhibit equant shapes (Fig.5e and Fig. 8d, e, f). The sample analyzed at the base of Unit I (SN-6; 28 mbsf) contains rare large clay-domain pores and abundant FF contacts (Fig. 5c; MAD porosity = 54% and COPL = 55%).

28 mbsf to 1500 mbsf (Units II and III)

Mud samples from the Nicobar fan section are more compacted than shallower samples (Fig. 6, 7 and Figure S8 in Supplementary data). We analyzed a total of 29 samples using at Aachen and 18 samples at UT Austin from this section. An increase in compactional strain from 2.00 to 3.15 over a depth range of 28 to 1500 mbsf causes a porosity reduction (MAD) of 54% to 28%, and the corresponding change in average COPL is 55% to 72%. The microstructure of these samples is dominated by FF contacts among clay particles; EF and EE contacts are rare (Table S4 in Supplementary data; Fig. 6 and 7 b, c). All samples exhibit abundant small linear-elongated clay domain pores between two parallel clay sheets (Fig. 8b). Equant-shaped small, clay domain pores are rarely observed below 150 mbsf depth ($\varepsilon_c > 2.4$). Crescent-shaped, small, clay domain pores are rare at shallow depth but become abundant with an increase in compactional strain $\varepsilon_c > 2.95$ (871.87 mbsf) as the surrounding clay particles are bent (Fig.6). In addition, large clay domain pores in these samples are rarely observed in the vicinity of silt clasts (Fig.6).

Below 100 mbsf ($\varepsilon_c = 2.20$), silt-adjacent small pores are dominantly equant shaped, but below 300 mbsf ($\varepsilon_c > 2.5$) silt-adjacent small pores are dominantly linear-elongated (Fig. 8e). Crescent-shaped, small, silt-adjacent pores are common in all samples. Large silt-adjacent pores are dominantly equant above 200 mbsf depth ($\varepsilon_c < 2.40$) and commonly linear-elongate below 400 mbsf depth ($\varepsilon_c > 2.5$) (Fig.8f). It appears that due to an increase in compactional strain, the shape of the silt-adjacent pores changes from equant to linear-elongated (Table S3 in Supplementary data). In samples with more silt, equant-shaped small and large, silt-adjacent pores can persist at greater depths (Fig. 8e and f).

Below 28 mbsf ($\varepsilon_c > 2.0$), the number of large silt-adjacent pores in the microstructures decreases. Comparing samples SN-8 (74.07 mbsf and $\varepsilon_c = 2.09$) and SN-33 (1299.14 mbsf and $\varepsilon_c = 2.51$) illustrates how the number of large, silt-adjacent pores decreases with depth (Fig. 6a, and c) when the clay fraction (Table S2 in Supplementary data) is comparable. This relationship is apparent even in samples separated by a smaller depth difference (SN-49 from 959.14 mbsf and SN-55 from 1433.36 mbsf; Fig. 7b and c). While the number of large pores diminishes, the maximum size of the large silt-adjacent pores remains constant (10^7 nm^2; Figure S9).

It can be observed in Fig.2e that, around 1300 mbsf depth MAD porosity for the sample sets again rapidly increases. However, microstructural observations of the sample from this horizon does not exhibit increase in porosity (Fig. 6c). Hence, the increase in MAD porosity in this horizon is attributed to the increase in smectite content (Fig.2a) (Dutilleul et al., 2021). In general, the moisture and density method (MAD) overestimate the measured porosity of the smectite rich sediment because of the inclusion of the interlayer water from smectite during measurement (Brown and Ransom, 1996; Dutilleul et al., 2020).

Variation in the orientation of pores and grains due to compactional strain

We examined the change in orientation of the long axis of pores with increasing compaction strain. For all segmented pores, the angle between the long axis and the bedding plane was determined and plotted in rose diagrams (Supplementary data-15). Samples from the seafloor to 28 mbsf exhibit a weak preferred orientation of the long axis of pores with maxima oriented obliquely to the bedding planes. However, below 28 mbsf the samples have a preferred orientation of the long axis of pores aligned subparallel to the bedding plane. Further, due to an increase in vertical effective stress down section below 28 mbsf in Units II and III, the degree of preferred alignment of the long axis of pores only increases by a small amount (Figure S10).

We determined the angle between the long axis of individual silt grains and the bedding plane for all samples and plotted the angle in a rose diagram (Figure S10). For quartz, feldspar, and calcite the degree of preferred orientation of the long axis of grains changes little with depth. However, the rose diagrams obtained for mica show weak maxima parallel to the bedding plane and several submaxima oriented obliquely to the bedding plane above 28 mbsf. Preferred alignment of the long axis of mica grains increases at 28 mbsf with a strong maximum oriented parallel to bedding plane. Below 28 mbsf, further increase in the degree of preferred alignment is small.

Size distribution of pores

Pore size distributions (Fig. 9) of shallow samples (Unit I) are trimodal. Sample SN-1 has peaks between 10^5 to 10^6 nm^2, 10^6 to 10^7 nm^2, and 10^7 to 10^8 nm^2, and SN-2 has peaks from 10^4 to 10^5 nm^2, 10^5 to 10^6 nm^2, and 10^6 to 10^7 nm^2. These three pore size regimes correspond to the small clay domain and silt-adjacent pores, large clay domain pores, and large silt-adjacent pores. Samples of Units II and III exhibit bimodal pore size distributions (SN-10, SN-26, and SN-33 in Fig. 9). SN-10 has a peak between 10^5 to 10^6 nm^2, corresponding to small clay domain and silt-adjacent pores, and 10^6 to 10^7 nm^2, reflecting large silt-adjacent pores. Large clay domain pores are absent from samples below 28 mbsf depth (Units II and III) based on the pore size distributions combined with image analysis. At shallow depths, the contribution to total porosity by larger silt-adjacent pores is greater compared to the contribution by small clay domain pores (Fig. 9e and g). The contribution of large, silt-adjacent pores to total porosity diminishes with depth. Hence, at greater depth, contribution to total porosity by larger silt adjacent pore is less compared to small clay domain pores (Fig. 9i).

Pore size distributions follow a power-law shown on a double logarithmic graph following the equations (Klaver et al., 2012; 2015; 2016; Hemes et al., 2013; 2015; 2016; Laurich et al., 2014):

$$\frac{N_i}{b_i S_{mosaic}} = C S_{Pore}{}^D \qquad \text{(Eqn-3)}$$

$$\log\left(\frac{N_i}{b_i S_{mosaic}}\right) = -D.\log(S_{pore}) + Log\ C \qquad \text{(Eqn-4)}$$

Where N_i= number of pores with area S_{pore}, b_i= bin size, S_{mosaic}= surface area of the current mosaic, C=constant, and D= power-law exponent. The resulting power-law exponent (D) varies between 1.70 to 2.00 (Table T2 in Supplementary data).

Effect of texture on porosity, pore morphology, and orientation of pores

We analyzed six samples (SN-7, SN-9, SN-17, SN-28, SN-29, and SN-31) that are enriched in silt content compared to the rest of the mud samples (Table T2 in Supplementary data)). Silt content has a positive correlation to the total SEM porosity. For example, sample SN-29 (1172.88 mbsf) exhibits a BIB-SEM porosity of 14% whereas other samples from a similar depth with less silt exhibit an average BIB-SEM porosity of 12% (Table T2 in Supplementary data)) at 20000x magnification. The samples with greater silt content are also enriched in equant-shaped silt-adjacent larger pores (Fig.10a). We also estimated the orientation of the long axis of pores for these three samples and plotted the obtained results as rose diagrams (Fig.10b). The obtained results exhibit a relatively weak preferred alignment of the long axis of pores with respect to the bedding planes (Fig.10b).

Discussions

Effective stress vs porosity: A comparison with experimental study

To understand the consolidation mechanisms of the Sumatra sediments, we estimated vertical effective stress following the steps proposed by Hüpers et al. (2015). Following Terzaghi and Peck (1948), vertical effective stress ($\sigma_v´$) is expressed as:

$$\sigma_v´ = \sigma_v - P_f \hspace{4cm} \text{(Eqn-5)}$$

Here σ_v = total vertical stress caused by the overburden load, and P_f = fluid pressure. To compute vertical effective stress of a layered sediment, we use Eqn 6:

$$\sigma_v´ = \sum(\boldsymbol{\rho_s} - \boldsymbol{\rho_w}).\, \mathbf{g}.\, \mathbf{\Delta z} \hspace{4cm} \text{(Eqn-6)}$$

where $\boldsymbol{\rho_s}$= bulk density of the sediment, $\boldsymbol{\rho_w}$= density of the pore water, Δz= depth interval, and g= gravitational acceleration. Although small offset strike-slip faults are evident at the seafloor and in seismic reflection profiles (McNeill et al., 2017a), the amount of strain attributed to these fault offsets supports the idea that the maximum horizontal stress is comparable to the vertical stress; there is no evidence in seismic reflection data or from core microstructures for thrust or reverse faults associated with a vertical least principal stress. On this basis, we assume that vertical stress is the maximum principal stress, and that pore pressure is hydrostatic. Bulk density of the sediment $\boldsymbol{\rho_s}$ was acquired from MAD data set obtained from IODP website (McNeill et al., 2017a), and $\boldsymbol{\rho_w}$ was considered as the density of seawater i.e. 1025 kg/m^3 (Hüpers et al., 2015).

We plotted vertical effective stress against MAD porosity for 55 mud samples (Fig.11). Fawad et al. (2010) experimentally studied the consolidation behavior of mud with varied proportions of silt and clay. While Sumatra samples follow trends like those defined by Fawad et al. (2010), the experimental samples are more compacted than natural Sumatra samples for the same silt content.

443 Clay mineralogy has a significant effect on the compaction behavior of mudstone (Mondol et al., 2007). Mondol
444 et al. (2007) performed compaction experiments using pure smectite and pure kaolinite clay particle packs because
445 they represent two end members compared to other clay minerals (illite and chlorite) in terms of grain size and
446 surface area. Smectite is the more fine-grained clay with the largest surface area while kaolinite is coarser and has
447 a smaller surface area than other clay mineral types (Meade, 1964; Mesri and Olson, 1971; Rieke and Chilingarian,
448 1974). Kaolinite is more compressible than smectite, and clay compaction gradually decreases with increasing the
449 proportion of small size clay particles in the sample (Mondol et al, 2007).

450 Fawad et al., (2010) used clay mixtures of 81% kaolinite, 14% mica, and 5% microcline grains, whereas Sumatra
451 mud samples are composed of 50%-79% illite and 5%-30% smectite, with only 8-20% undifferentiated chlorite
452 and kaolinite and 5-10% quartz particles. Therefore, due to higher illite and smectite content, Sumatra muds
453 appeared to be less compacted than the experimental samples used by Fawad et al. (2010).

BIB-SEM porosity vs MAD porosity

455 We note that BIB-SEM porosity is lower than the porosity found from shipboard MAD data, however the two
456 measurements correlate along a line through the origin. (Fig.3b). The reason for this difference is that MAD
457 porosity measures the total amount of moisture in a much larger sample and accounts for pores much below the
458 PPR. Rare large pores are also under-represented in the 1 mm^2 BIB section. Earlier studies also documented and
459 discussed mismatches between MAD and BIB-SEM measurements (Hemes et al., 2013; Houben et al., 2014; Nole
460 et al., 2016; Oelker et al., 2019). They concluded that the mismatch could be due to several factors; i) BIB-SEM
461 porosity largely depends on the magnification and resolution of images, ii) variation in sample sizes, and iii) MAD
462 porosity takes into account the pores whose sizes are much lower than PPR, whereas BIB-SEM technique detects
463 only the pores larger than PPR. We plotted estimated BIB-SEM porosity and MAD porosity data from earlier
464 studies on Boom clay (Hemes et al., 2013; Oelker et al., 2019); Opalinus clay (Houben et al., 2014) and samples
465 from the Nankai trough (Nole et al., 2016). The data for Boom clay and Opalinus clay follow a similar trend to the
466 Sumatra samples, whereas clay samples from the Nankai trough shows a different trend. This difference may be
467 attributed to differences in magnification of Nankai trough samples.

468 In addition, we plotted clay content against the difference between the two porosities in Fig.12a. We performed
469 regression analysis using the data set for the 33 mud samples analyzed at Aachen (Fig.12b) for BIB-SEM porosity
470 versus MAD porosity (following Eqn-7) but also incorporating the effect of clay content (following the Eqn-8).

471 BIB-SEM porosity=a*MAD porosity + c   (Eqn-7)

472 BIB-SEM porosity =a*MAD porosity + b*clay content + c   (Eqn-8)

473 The coefficient of determinations (R^2) for Eqn-7 and Eqn-8 are 0.7126 and 0.9262 respectively. These results
474 suggest that the ratio in porosity depends on depth and clay content.

475 For all samples, the BIB-SEM pore size distribution follows a power-law over an interval of three orders of
476 magnitude. We may extrapolate this below the practical pore resolution (PPR; Klaver et al., 2012; Kuila and

Prasad, 2013; Wang et al., 2019). Extrapolating our data set down to 3 nm pore diameter, the BIB-SEM porosity increases only up to 20%~25%. A mismatch of 15% to 20% between the MAD porosity and extrapolated BIB-SEM porosity remains. The fall -off from the normal trend in log-log pore size distribution plots (Fig.9b) for the shallow depth (Unit-I) samples suggest that also large pores are also under-counted in the data set. The mud samples from Unit-I contains forams that are rare or absent in the deeper section (Figure S11 a, b, c, and d in Supplementary data), and part of missing pore volume can be attributed to the intact forams that may be missed due to the small size of the BIB SEM sample.

Another factor that can create a mismatch between data sets is drying artefacts. In the past, Desbois et al. (2014) performed a detailed study on drying artefacts of mudstone samples using Cryogenic BIB-SEM technique. They identified four types of drying damages (Type-I, II, III and IV) that can develop during drying of a mudstone. Type-I and type-II drying damage develops at clay/clay particle interfaces with tip to long axis contact, and at clay/clast interfaces. Heterogeneous deformational behavior or shrinkage strain of clay and/or non-clay mineral grains can cause a build-up in stress at the boundary between particles during drying. Type-III drying artefacts are large cracks that develops within the clay matrix itself. Type-IV drying artefacts are the small damages that modify pore morphology during drying. Among all of them, Type-II and III are the most spectacular and large enough to modify microstructure significantly. The morphology of the type-II and III drying artefacts are characterized by large irregular shaped very elongated pores with serrated pore boundaries. However, in the present study, the large clay domains and silt-adjacent pores in all samples potentially show smooth edges and rounded pore tip-end, which are incompatible with the typical morphologies of the drying artefacts (Fig. 5, 6 and 7). Hence, drying artefacts appear to be less important for reconciling a mismatch between MAD and BIB-SEM porosity.

Shallow samples from Unit-I are richer in smectite content than deeper samples, although a few samples from 400 to 1000 mbsf have similar smectite abundances as Unit I. The moisture and density method (MAD) may overestimate the measured porosity of the sediment if interlayer water from smectite is included in the measurement (Brown and Ransom, 1996; Dutilleul et al., 2020). Greater smectite content in the shallow samples (Unit-I) may have contributed to an overestimation of the MAD porosity in the study. This is also consistent with the observation that the difference between the measurements getting larger as porosity increases.

Micromechanical model for porosity reduction

Sharp reduction in porosity at the shallow depth from the seafloor to 28 mbsf

High porosity (80% MAD; 32% BIB-SEM) in the shallowest sediments is attributed to large pores in the samples created by abundant EE and EF particle contacts (Fig. 5a and 7a). These contacts are unstable and collapse under low effective stress to form FF contacts, resulting in a rapid porosity decrease within the first 28m of burial (Supplementary data-11). This deformation is apparent from the reduction of large clay domain pores observed over this interval (Fig. 8; Supplementary data-10). Collapse of pores surrounded by EE and EF contacts is further recognized by the progressive alignment of clay particles into the bedding plane, which promotes an increase in the number of elongated, small, clay domain pores parallel to the bedding plane. Each of these observations is consistent with rotation of clay particles into the bedding plane as these large clay-domain pores collapse.

Mechanism of porosity reduction from 28 mbsf to 1500 mbsf

Below 28 mbsf to >1500 mbsf, porosity continues to decrease from 52-30% (MAD) but at a reduced pace. SEM observations suggest that this porosity decline results from the progressive loss of silt-adjacent pores with large silt-adjacent pores lost before small ones (Fig. 8), although they remain present in common abundance to 1200 mbsf. Small clay domain pores are abundant throughout the section, and the large clay domain pores are lost between the seafloor and 28 mbsf.

Within the population of silt-adjacent pores, the large, equant pores are most susceptible to collapse (Fig. 8). Large, elongate pores persist in abundance, both in linear and crescent geometries. While it seems plausible that large, equant pores collapse to form large, elongate pores, no corresponding increase in the elongate pore population is observed. Large, elongate pores may collapse further and become small silt-adjacent pores. Microstructural evidence supports the idea that large equant pores collapse as surrounding clay particles within clay-rich domains bend and shrink the size of the remaining pore (Fig.13), and that the collapse results in an increasing aspect ratio of the pore.

Frequently, bent clay particles are observed on the top of larger silt-adjacent pores. In the clay microstructure, large silt-adjacent pores act as a zone of heterogeneous strain localization. Clay particles can bend and collapse into large silt-adjacent pores more readily than the smaller pores in the clay matrix (Fig.13a to f). With increasing vertical effective stress two situations can arise which are demonstrated in the model shown in Fig.13g. First, with an increase in effective stress, the bent clay particles can lose frictional resistance from the sidewall (Fig.13a and b), can continue to bend, and slide down to fill the larger silt-adjacent pore space (Fig.13g-(iii)). Second, with an increase in vertical effective stress, bent clay particles may develop fractures (red lines in Fig.13g-(iv)) and subsequently collapse into the larger silt-adjacent pore space to reduce the porosity of samples (Fig.13g-(v)). Fig.13a represents fractured bent clay on the top of the larger silt adjacent pore (shown by white arrow). Similarly, two small clay particles appear to have fallen into the larger silt adjacent pore space (Fig.13e) while another bent clay particle (shown by white arrow) covers the pore. Fig.13f represents a bent clay particle wrapping across the top of two quartz particles, and four small clay platelets fill the space between two quartz particles, suggesting an older, larger silt-adjacent pore filled by fractured clay platelets. Occurring within the pore space between two equant quartz grains (Fig.13f), four small clay particles appear to have developed due to the fracturing of two large bent clay particles. Hence, it appears that the collapse of larger silt-adjacent pores in these mud samples is governed by the bending of clay particles and subsequent fracturing due to an increase in vertical effective stress. While these processes are defined within individual pores, the observed deformation is interpreted to result from an imposed force chain that acts on specific pores in a progressive manner as the force chain evolves and as adjacent pores deform.

Small silt-adjacent pores also become less abundant with burial, but the transition occurs deeper than the large pores, and small, silt-adjacent pores remain common throughout the section (Fig. 8; Supplementary data-11). Small equant pores are lost like the large pores, and elongate pores remain abundant within this population subset throughout. There is a loose correspondence between the loss of small, equant pores and an increase in elongate

549 pores, suggesting that pore flattening is part of the pore collapse history. The pore collapse evolution outlined for

550 large pores (Fig.13g) appears to also hold for small pores, even though observations are more challenging.

551 Small, clay domain pores appear to remain resilient throughout the compaction history (Fig. 8), even though some

552 of these pores must become lost to account for porosity loss. Small, equant pores are lost between 100-200 m, and

553 this loss appears to be accommodated by an increase in elongate pores (Fig. 8). Elongate crescent pores increase

554 in abundance around 800 mbsf, and we interpret this to reflect folding of abundant linear elongate pores as the

555 overall system compacts.

556 Large equant pores in the clay domain are lost within the first few 10's of meters of burial. Elongate pores appear

557 to form at the expense of equant pores, and there may be a reduction in pore size associated with this shape change.

558 Most of the pores remaining after 1500 m of burial are small, elongate pores found both in clay domain and silt-

559 adjacent pores.

560 The presence of silt particles locally redistributes the force chain of load to retain undeformed, silt-adjacent, large

561 pores (Schneider et al., 2011). The samples with greater silt content are also enriched in equant-shaped silt-adjacent

562 larger pores (Fig.10) in the microstructure. Hence, as a result, they display greater porosity compared to other

563 samples from similar depth intervals (Fig.10).

564 Previous studies report contrasting ideas on the development of phyllosilicate fabric strength due to mechanical

565 compaction. Some studies suggest that mechanical compaction creates a phyllosilicate fabric in mud (Bowles et

566 al., 1969; Oertel and Curtis, 1972; Vasseur et al., 1995), whereas other studies conclude that vertical effective

567 stress has limited impact on phyllosilicate fabric development (Ho et al., 1999; Aplin et al., 2006; Day-Stirrat et

568 al., 2008; 2011). Here, we consider the preferred orientation of pores as a proxy for the alignment of phyllosilicate

569 (Hemes et al., 2013). At shallow depth (Unit-I), a weak preferred alignment of the long axis of pores with maxima

570 oriented obliquely to the bedding planes is formed (Supplementary data-15), and at greater depth (Unit-II and III)

571 the long axes of pores become aligned subparallel to the bedding plane. Increase in vertical effective stress below

572 28 mbsf depth creates only a small increase in the preferred orientation of the long axis of pores. Hence, we found

573 only a limited change in phyllosilicate fabric strength with increasing vertical stress..

574 Previous authors also document the evolution of pore size distribution in mud with an increase in consolidation

575 stress using laboratory experiments and merury-intrusion porosimetry (Griffiths and Joshi, 1989; 1990). They

576 conclude that the pore size distribution appears to be bi-modal, and the distribution curve shifts toward smaller

577 pore sizes with an increase in applied consolidation stress (Griffiths and Joshi, 1989). We observe an initial

578 transition from tri-modal to bi-modal pore size distribution around 28 mbsf depth due to rapid collapse of large

579 clay domain pores by compactional strain. With an increase in depth below 28 mbsf, the bi-modal pore size

580 distribution persists and tends to shift toward small pore sizes as the number of larger silt-adjacent pores

581 diminishes.

582 Laboratory studies have emphasized the importance of clay particle rotation as a dominant mechanism for

583 mechanical compaction in mudstone (Bennett et al., 1981, 1991; Vasseur et al., 1995; Aplin et al., 2006; Day-

584 Stirrat et al., 2008; 2011). We observe particle rotation only in the shallowest samples where unstable EE and EF

585 particle contacts are present. Clay particle bending and sliding/fracturing are considered more important for most
586 of the section studied.

Mechanical compaction of marine sediment: a conceptual model

588 According to earlier studies (Delage and Lefebvre, 1984; Griffiths and Joshi, 1989; 1990; Emmanuel and Day-
589 Stirrat 2012), the reduction of pores in sedimentary rocks during compaction is size-dependent - larger pores
590 deform much readily than smaller pores. According to their model, larger pores rapidly decrease in size during
591 compaction to reduce the overall porosity of the sample. However, microstructural analysis of Sumatra samples
592 suggests that porosity reduction is accomplished by compaction of all pore sizes. Moreover, the maximum size of
593 pores remains almost constant irrespective of increasing vertical effective stress/depth (Supplementary data-8)
594 with little difference observed for the maximum pore size in samples from 98.25 mbsf and 1299.31 mbsf. The
595 preservation of a constant ratio between MAD and BIB-SEM porosity measurements (Fig. 3b) suggests that
596 porosity loss is distributed across all pore sizes. We infer that all pore sizes are available for compaction for every
597 increment of applied stress but acknowledge that pore size reduction in different size classes may proceed at
598 different rates.

599 We propose a new model for the reduction in porosity in which all pores within the force chain of load take part
600 in the reduction of porosity during compaction irrespective of their size. At shallow depth up to 28mbsf, larger
601 clay-domain pores are the most susceptible to early response during an increase in compactional strain, because of
602 two reasons: 1) the 'domains' defined by the clay particles are weaker compared to the larger, rigid silt grains, and
603 2) due to higher relative proportion of clay-rich regions within the mud, the force chain of load dominantly passes
604 through the clay domains. The dispersed nature of the silt-size particles and the high proportion of phyllosilicates
605 in the mud samples indicate that soft clay particles act as the principal load-bearing framework. Hence, larger clay
606 domain pores are more unstable compared to silt-adjacent pores in the mud microstructure. Similarly, below
607 28mbsf depth, under an increase in vertical effective stress, both the larger silt-adjacent pores and smaller pores in
608 the clay matrix that come within the force chain of load collapse. Hence, the ratio between BIB-SEM porosity vs
609 MAD porosity remains almost constant irrespective of the depth. All larger silt-adjacent pores do not come within
610 the force chain of load at the same time. Hence, some of the larger silt-adjacent pores remained undeformed to the
611 maximum depth of 1500mbsf depth. Therefore, the maximum size of the larger silt-adjacent pores remains almost
612 constant irrespective of the depth/vertical effective stress.

613 In this study, we investigated how systematically pore types evolve with increasing depth in naturally compacted
614 samples. However, tracking the pore evolution through additional size categories would elucidate the pore
615 evolution in more detail. Preliminary pore size distribution data (Fig.9) indicate that 4 size bins exist in these
616 samples. Developing this approach requires improved image analysis techniques to tie all the pore attributes
617 together on a pore-by-pore basis for a huge number of pores.

Compaction strain accommodation and grain-scale deformation

619 Deformation of clay-rich sedimentary rocks involves four possible mechanisms: 1) Particulate flow; (Morgenstern
620 and Tchalenko, 1967; Borradaile et al., 1981); 2) Cataclasis; (Ukar and Cloos, 2019) 3) Diffusive mass transfer;

621 (Blenkinsop, 2007; Fossen, 2016); 4) Intercrystalline plasticity (Blenkinsop, 2007; Fossen, 2016). Intensity and
622 occurrence of a particular deformation mechanism in a mudstone depend on several parameters, such as effective
623 stress, water content, cementation, temperature (Desbois et al., 2017; Den Hartog and Spiers, 2014).

624 All our samples show evidence of particulate flow controlled by friction between grains. At shallow depths, illite
625 platelets contacted at EE and EF junctions lose these weak bonds, and particles rotate into bedding-parallel
626 orientation. Once FF contacts dominate, large-scale rotations are reduced, and inter-particle slip becomes
627 important. This is best evidenced in collapse of large, silt-adjacent pores where bent clay particles overlay pores
628 (Fig.14a to f). In deforming granular foam material, bending was reported as the dominant deformation mechanism
629 for the reduction in porosity and developing preferred alignment of the long axis of pores perpendicular to the
630 applied stress (Elliott et al., 2002, Zhou et al., 2004; Samsudin et al., 2017; Zakaria et al., 2018) (review of these
631 earlier studies on the experimental deformation of granular foam is described in document S2). Friction adheres
632 clay particles to the edge of pores while the middle of particles drops into the pore, resulting in bending by intra-
633 particle slip. A cartoon (Fig.14g) illustrates the compaction mechanism associated with the bending of clay
634 particles. With increasing compaction strain, clay particles undergo bending, and as a result, pore area reduces,
635 and the orientation of the pores tends to align perpendicular to the applied effective stress (Fig.14g). At shallow
636 depths (Unit-I), particles get enough free space for rotation to align parallel to the bedding plane because of higher
637 porosity (Figure S12a and b). However, at greater depth where porosity decreases, space problems limit particle
638 deformation to bending and fracturing as increase in compactional strain increases (Figure S12c and d).

Compaction of Sumatra input section: generalized implication for rock property evolution

641 The overall compaction curve obtained for Sumatra muds is comparable with the experimental study by Fawad et
642 al., 2010 in the context of compactional range (Fig.8). The curve shows a mono-exponential decrease in porosity
643 with an increase in vertical effective stress, which is evidence of normal consolidation (Fawad et al., 2010;
644 Dutilleul et al., 2020).

645 The larger silt-adjacent pores seen in the deepest of these samples (1500 m burial) suggest these muds retain
646 considerable potential for additional mechanical compaction with deeper burial. As this marine sediment
647 progressively approaches greater burial closer to the accretionary prism, it will undergo further change in physical
648 and deformational properties (Bray and Karig, 1985). Despite the substantial compactional strain, the relatively
649 high porosity of the deepest sample and the survival of larger and mechanically unstable silt-margin pores suggests
650 that compactional stabilization has yet to be reached because such IGVs and pore types are not generally observed
651 in older and lithified mudrocks. Based on the current understanding of subduction zone deformation behavior and
652 mudrock properties, it seems likely that mechanical compaction will continue to dominate the pore loss in deeper
653 burial.

654 The general absence of early cementation and the corresponding dominance of mechanical compaction in the total
655 pore loss is consistent with observations of other siliciclastic-dominated muds (Milliken, 2014; 2019). The trends
656 for intergranular volume change observed from the seafloor and 1500 mbsf place useful constraints on the

maximum cement volumes that theoretically could be emplaced at this depth range in sediments containing a more reactive grain assemblage. At the depths of burial attained at the deformation front, any cementation of the Sumatra input sediments will be limited to <30% of the rock volume, or possibly much less, as mechanical compaction is expected to continue up to the burial temperatures that initiate grain reactions and associated cementation.

Conclusions

Pores are classified by size and microstructural position, resulting in a multi-modal contribution to the total porosity. Shallow samples (seafloor to 28 mbsf) display a sharp reduction in porosity from 80% to 52% as large clay domain/matrix pores collapse. Deeper samples (28 mbsf to 1500 mbsf) exhibit a smaller reduction in porosity from 50% to 32% due to the collapse of silt-adjacent pores by bending and subsequent fracturing/sliding of clay particles.

The class of large pores next to silt-sized grains (between 10^4 and 10^6 nm^2) remains common to >1 km burial, irrespective of the mineralogy of the silt-sized grains, but their size decreases with depth. Small, equant pores next to silt particles are abundant in the first 100 m of burial and remain common over the entire depth range.

Small pores in clay domains are almost all elongated, and abundant over all observed depths. Small, crescent-shaped elongate pores increase in abundance with depth as clay particles become folded by compactional processes.

The size-independence of pore loss arises because the force chain driving pore collapse is localized primarily within the volumetrically dominant and weaker clay-rich domains; larger pores around isolated silt particles enter into the force chain somewhat randomly and asynchronously and do not contribute preferentially to pore loss over the depth range studied.

An increase in effective stress up to 18 MPa (~1500 mbsf) causes the development of weakly aligned phyllosilicate fabric (defined by mica and illite clay particles) in the microstructure.

Compaction processes in our samples are dominated by granular flow (rotation and frictional sliding of illite clay particles) at shallow depths. With increasing depth, compaction is additionally accommodated by bending of clay particles.

Data availability

High resolution SE2 and BSE images of all samples are available online at:
https://figshare.com/s/cbaada517b0b1409d575

Authors contributions

SL and KLM performed sample preparation and BIB-SEM microscopy. SL analysed the data. JLU and GD acquired funding. JLU managed the project. PV, KLM and JLU significantly contributed to interpret the data. SL

wrote the first draft of the manuscript. PV, KLM and JLU contributed for the correction and improvement of the manuscript.

Competing interests

The authors declare that they do not have any conflict of interest.

Acknowledgments

SL and JLU thank German Research Foundation (Deutsche Forschungsgemeinschaft [DFG] grant UR 64/19-1) for providing funding to carry out the research. IODP (International Ocean Discovery Programme) sample repository, Japan is acknowledged for providing oriented mud samples for the study. KLM acknowledges the samples and data provided by the International Ocean Discovery Program (IODP). Funding for sample preparation and SEM imaging was supported by a post-expedition award (Milliken, P.I.) from the Consortium for Ocean Leadership. SL thanks Manuel Menzel, Jop Klaver, Liene Spruženiece, and Joyce Schmatz for providing valuable time to teach BIB-SEM techniques. We would like to thank Dave Dewhurst and Bernhard Schuck for their constructive ideas in the review reports, and Virginia Toy for editorial handling.

References

Adams, R. and Bischof, L.: Seeded region growing. IEEE Transactions on pattern analysis and machine intelligence. IEEE: 16(6), 641-647. https//DOI. 10.1109/34.295913, 1994.

Ajdukiewicz, J. M. and Lander, R. H.: Sandstone reservoir quality prediction: state of the art, AAPG Bulletin, 94,: 1082-1091, https:// doi.org/10.1306/intro060110, 2010.

Ammon, C.J., Ji, C., Thio, H.K., Robinson, D., Ni, S., Hjorleifsdottir, V., Kanamori, H., Lay, T., Das, S., Helmberger, D. and Ichinose, G. Rupture process of the 2004 Sumatra-Andaman earthquake, Science, 308(5725), 1133-1139, DOI: 10.1126/science.1112260, 2005.

Aplin, A.C. and Macquaker, J.H.: Mudstone diversity: Origin and implications for source, seal, and reservoir properties in petroleum systems, AAPG bulletin, 95(12), 2031-2059, https://doi.org/10.1306/03281110162, 2011.

Aplin, A.C., Matenaar, I.F. and Vvan Dder Pluijm, B.A.: Influence of mechanical compaction and chemical diagenesis on the microfabric and fluid flow properties of Gulf of Mexico mudstones Journal of Geochemical Exploration, 78, 449-451, https://doi.org/10.1016/S0375-6742(03)00035-9, 2003.

Aplin, A.C., Matenaar, I.F., McCarty, D.K. and Vvan Der Pluijm, B.A.: Influence of mechanical compaction and clay mineral diagenesis on the microfabric and pore-scale properties of deep-water Gulf of Mexico mudstones, Clays and Clay Minerals, 54(4), 500-514, https://doi.org/10.1346/CCMN.2006.0540411, 2006.

717   Backman, J., Chen, W., Kachovich, S., Mitchison, F. L., Petronotis, K. E., Yang, T. and Zhao, X.: Data report:
718   Revised age models for IODP Sites U1480 and U1481, Expedition 362, Proceedings of the International Ocean
719   Discovery Program, Expedition Reports 362, https://doi.org/10.14379/iodp.proc.362.202.2019, 2019.

720   Baruch, E.T., Kennedy, M.J., Löhr, S.C. and Dewhurst, D.N.: Feldspar dissolution-enhanced porosity in
721   Paleoproterozoic shale reservoir facies from the Barney Creek Formation (McArthur Basin, Australia). AAPG
722   Bulletin, 99(9), 1745-1770, https://doi.org/10.1306/04061514181, 2015.

723   Bennett, R.H., Bryant, W.R. and Keller, G.H.: Clay fabric of selected submarine sediments; fundamental properties
724   and models, Journal of Sedimentary Research, 51(1), 217-232, https://doi.org/10.1306/212F7C52-2B24-11D7-
725   8648000102C1865D, 1981.

726   Bennett, R.H., O'Brien, N.R. and Hulbert, M.H.: Determinants of clay and shale microfabric signatures: processes
727   and mechanisms. In Microstructure of Fine-Grained Sediments, 5-32, Springer, New York, NY. https://DOI:
728   10.1007/978-1-4612-4428-8_2, 1991.

729   Blenkinsop, T.G.: Deformation microstructures and mechanisms in minerals and rocks, Springer Science &
730   Business Media, 2007.

731   Bowles, F.A., Bryant, W.R. and Wallin, C.: Microstructure of unconsolidated and consolidated marine sediments,
732   Journal   of   Sedimentary   Research,   39(4),   1546-1551,   https://doi.org/10.1306/74D71E7E-2B21-11D7-
733   8648000102C1865D, 1969.

734   Borradaile, G.J.: Particulate flow of rock and the formation of cleavage. Tectonophysics, 72(3-4), 305-321,
735   https://doi.org/10.1016/0040-1951(81)90243-2, 1981.

736   Bray, C.J. and Karig, D.E.: Porosity of sediments in accretionary prisms and some implications for dewatering
737   processes, Journal   of   Geophysical   Research: Solid   Earth,   90(B1),   768-778,   https://doi.org/
738   10.1029/JB090iB01p00768, 1985.

739   Brown, K.M. and Ransom, B.: Porosity corrections for smectite-rich sediments: Impact on studies of compaction,
740   fluid   generation,   and   tectonic   history. Geology, 24(9),   843-846,   https://doi.org/10.1130/0091-
741   7613(1996)024<0843:PCFSRS>2.3.CO;2, 1996.

742   Burland, J.B.: On the compressibility and shear strength of natural clays. Géotechnique, 40(3), 329-378,
743   doi.org/10.1680/geot.1990.40.3.329, 1990.

744   Chester, F.M., Rowe, C., Ujiie, K., Kirkpatrick, J., Regalla, C., Remitti, F., Moore, J.C., Toy, V., Wolfson-
745   Schwehr, M., Bose, S. and Kameda, J.: Structure and composition of the plate-boundary slip zone for the 2011
746   Tohoku-Oki earthquake. Science, 342(6163), 1208-1211, https://DOI: 10.1126/science.1243719, 2013.

747   Cetin, H.: Soil-particle and pore orientations during consolidation of cohesive soils. Engineering geology, 73(1-
748   2), 1-11, doi.org/10.1016/j.enggeo.2003.11.006, 2004.

749 Day-Stirrat, R.J., Aplin, A.C., Środoń, J. and Van der Pluijm, B.A.: Diagenetic reorientation of phyllosilicate
750 minerals in Paleogene mudstones of the Podhale Basin, southern Poland, Clays and Clay Minerals, 56(1), 100-
751 111, DOI: 10.1346/CCMN.2008.0560109, 2008.

752 Day-Stirrat, R.J., Flemings, P.B., You, Y., Aplin, A.C. and van der Pluijm, B.A.: The fabric of consolidation in
753 Gulf of Mexico mudstones, Marine Geology, 295, 77-85, https://doi.org/10.1016/j.margeo.2011.12.003, 2012.

754 Day-Stirrat, R.J., Milliken, K.L., Dutton, S.P., Loucks, R.G., Hillier, S., Aplin, A.C. and Schleicher, A.M.: Open-
755 system chemical behavior in deep Wilcox Group mudstones, Texas Gulf Coast, USA, Marine and Petroleum
756 Geology, 27(9), 1804-1818, https://doi.org/10.1016/j.marpetgeo.2010.08.006, 2010.

757 Day-Stirrat, R.J., Schleicher, A.M., Schneider, J., Flemings, P.B., Germaine, J.T. and van der Pluijm, B.A.:
758 Preferred orientation of phyllosilicates: Effects of composition and stress on resedimented mudstone
759 microfabrics, Journal of Structural Geology, 33(9), 1347-1358, https://DOI:10.1016/j.jsg.2011.06.007, 2011.

760 Dean, S.M., McNeill, L.C., Henstock, T.J., Bull, J.M., Gulick, S.P., Austin, J.A., Bangs, N.L., Djajadihardja, Y.S.
761 and Permana, H.: Contrasting décollement and prism properties over the Sumatra 2004–2005 earthquake rupture
762 boundary, Science, 329(5988), 207-210, https://DOI: 10.1126/science.1189373, 2010.

763 Delage, P. and Lefebvre, G.: Study of the structure of a sensitive Champlain clay and of its evolution during
764 consolidation. Canadian Geotechnical Journal, 21(1), 21-35, https://doi.org/10.1139/t84-003, 1984.

765 Delle Piane, C., Almqvist, B.S., MacRae, C.M., Torpy, A., Mory, A.J. and Dewhurst, D.N.: Texture and diagenesis
766 of Ordovician shale from the Canning Basin, Western Australia: Implications for elastic anisotropy and
767 geomechanical properties. Marine and Petroleum Geology, 59, 56-71, doi.org/10.1016/j.marpetgeo.2014.07.017,
768 2015.

769 Den Hartog, S. A. and Spiers, C. J.: A microphysical model for fault gouge friction applied to subduction
770 megathrusts, Journal of Geophysical Research: Solid Earth, 119(2), 1510-1529.
771 https://doi.org/10.1002/2013JB010580, 2014.

772 Desbois, G., Urai, J.L. and Kukla, P.A.: Morphology of the pore space in claystones–evidence from BIB/FIB ion
773 beam sectioning and cryo-SEM observations. eEarth Discussions, 4(1), 1-19, 2009.

774 Desbois, G., Urai, J.L., Hemes, S., Brassinnes, S., De Craen, M. and Sillen, X.: Nanometer-scale pore fluid
775 distribution and drying damage in preserved clay cores from Belgian clay formations inferred by BIB-cryo-
776 SEM. Engineering Geology, 179, 117-131, https://doi.org/10.1016/j.enggeo.2014.07.004, 2014.

777 Desbois, G., Höhne, N., Urai, J. L., Bésuelle, P., and Viggiani, G.: Deformation in cemented mudrock (Callovo–
778 Oxfordian Clay) by microcracking, granular flow and phyllosilicate plasticity: insights from triaxial deformation,
779 broad ion beam polishing and scanning electron microscopy, Solid Earth, 8, 291–305, https://doi.org/10.5194/se-
780 8-291-2017, 2017.

781   Desbois, G., Urai, J. L., Kukla, P. A., Konstanty, J., & Baerle, C.: High-resolution 3D fabric and porosity model
782   in a tight gas sandstone reservoir: A new approach to investigate microstructures from mm-to nm-scale combining
783   argon beam cross-sectioning and SEM imaging. Journal of Petroleum Science and Engineering, 78(2), 243-257,
784   https://doi.org/10.1016/j.petrol.2011.06.004, 2011.

785   Djeran-Maigre, I., Tessier, D., Grunberger, D., Velde, B. and Vasseur, G.: Evolution of microstructures and of
786   macroscopic properties of some clays during experimental compaction. Marine and Petroleum Geology, 15(2),
787   109-128, doi.org/10.1016/S0264-8172(97)00062-7, 1998.

788   Dugan, B., McNeill, L. and Petronotis, K.: Expedition 362 preliminary report: Sumatra subduction zone,
789   International Ocean Discovery Program, 2017.

790   Dutilleul, J., Bourlange, S., Conin, M. and Géraud, Y.: Quantification of bound water content, interstitial porosity
791   and fracture porosity in the sediments entering the North Sumatra subduction zone from Cation Exchange Capacity
792   and   IODP   Expedition   362   resistivity   data, Marine   and   Petroleum   Geology, 111,   156-165,.
793   https://doi.org/10.1016/j.marpetgeo.2019.08.007, 2020.

794   Ehrenberg, S. N.: Assessing the relative importance of compaction processes and cementation to reduction of
795   porosity in sandstones: discussion. American Association of Petroleum Geologists Bulletin, 73, 1274-1276,
796   https://doi.org/10.1306/44B4AA1E-170A-11D7-8645000102C1865D, 1989.

797   Elliott, J.A., Windle, A.H., Hobdell, J.R., Eeckhaut, G., Oldman, R.J., Ludwig, W., Boller, E., Cloetens, P. and
798   Baruchel, J.: In-situ deformation of an open-cell flexible polyurethane foam characterised by 3D computed
799   microtomography, Journal of materials science, 37(8), 1547-1555, doi:10.1023/A:1014920902712, 2002.

800   Emmanuel, S. and Day-Stirrat, R.J.: 2012. A framework for quantifying size dependent deformation of nano-scale
801   pores in mudrocks Journal of applied geophysics, 86, 29-35, https://doi.org/10.1016/j.jappgeo.2012.07.011, 2012.

802   Fawad, M., Mondol, N.H., Jahren, J. and Bjørlykke, K.: Microfabric and rock properties of experimentally
803   compressed   silt-clay   mixtures, Marine   and   Petroleum   Geology, 27(8),   1698-1712,
804   https://doi.org/10.1016/j.marpetgeo.2009.10.002, 2010.

805   Fossen, H.: Structural geology. Cambridge university press. 2016.

806   Ghosal, D., Singh, S.C. and Martin, J.: Shallow subsurface morphotectonics of the NW Sumatra subduction system
807   using   an   integrated   seismic   imaging   technique, Geophysical   Journal   International, 198(3),   1818-1831,
808   https://doi.org/10.1093/gji/ggu182, 2014.

809   Griffiths, F.J. and Joshi, R.C.: Change in pore size distribution due to consolidation of clays. Geotechnique, 39(1),
810   159-167, doi.org/10.1680/geot.1989.39.1.159, 1989.

811   Griffiths, F.J. and Joshi, R.C.: Clay fabric response to consolidation. Applied clay science, 5(1), 37-66,
812   doi.org/10.1016/0169-1317(90)90005-A, 1990.

813   Griffiths, F.J. and Joshi, R.C.: Change in pore size distribution owing to secondary consolidation of
814   clays. Canadian Geotechnical Journal, 28(1), 20-24, https://doi.org/10.1139/t91-003, 1991.

815   Hemes, S., Desbois, G., Klaver, J. and Urai, J.L.: Microstructural characterisation of the Ypresian clays (Kallo-1)
816   at nanometre resolution, using broad-ion beam milling and scanning electron microscopy. Netherlands Journal of
817   Geosciences, 95(3), 293-313, DOI: https://doi.org/10.1017/njg.2016.16, 2016.

818   Hemes, S., Desbois, G., Urai, J.L., De Craen, M. and Honty, M.: Variations in the morphology of porosity in the
819   Boom Clay Formation: insights from 2D high resolution BIB-SEM imaging and Mercury injection
820   Porosimetry. Netherlands Journal of geosciences, 92(4), 275-300, DOI: doi.org/10.1017/S0016774600000214,
821   2013.

822   Hemes, S., Desbois, G., Urai, J.L., Schröppel, B. and Schwarz, J.O.: Multi-scale characterization of porosity in
823   Boom Clay (HADES-level, Mol, Belgium) using a combination of X-ray μ-CT, 2D BIB-SEM and FIB-SEM
824   tomography. Microporous and mesoporous materials, 208, 1-20, https://
825   doi.org/10.1016/j.micromeso.2015.01.022, 2015.

826   Hesse, R.: Turbiditic and non-turbiditic mudstone of Cretaceous flysch sections of the East Alps and other
827   basins. Sedimentology, 22(3), 387-416, https://doi.org/10.1111/j.1365-3091.1975.tb01638.x, 1975.

828   Hippchen, S. and Hyndman, R.D.: Thermal and structural models of the Sumatra subduction zone: Implications
829   for the megathrust seismogenic zone. Journal of Geophysical Research: Solid Earth, 113(B12), https://doi.org/10.
830   https://doi.org/10.1002/2015TC003901, 2008.

831   Ho, N.C., Peacor, D.R. and Van der Pluijm, B.A.: Preferred orientation of phyllosilicates in Gulf Coast mudstones
832   and relation to the smectite-illite transition. Clays and Clay Minerals, 47(4), 495-504, DOI: 10.1346/CCMN.
833   1999.0470412, 1999.

834   Houben, M.E., Desbois, G. and Urai, J.L.: A comparative study of representative 2D microstructures in Shaly and
835   Sandy facies of Opalinus Clay (Mont Terri, Switzerland) inferred form BIB-SEM and MIP methods, Marine and
836   Petroleum Geology, 49, 143-161, https://doi.org/10.1016/j.marpetgeo.2013.10.009,. 2014.

837   Hüpers, A., Ikari, M.J., Dugan, B., Underwood, M.B. and Kopf, A.J.: Origin of a zone of anomalously high
838   porosity in the subduction inputs to Nankai Trough. Marine Geology, 361, 147-162,
839   https://doi.org/10.1016/j.margeo.2015.01.004, 2015.

840   Hüpers, A., Torres, M.E., Owari, S., McNeill, L.C., Dugan, B., Henstock, T.J., Milliken, K.L., Petronotis, K.E.,
841   Backman, J., Bourlange, S. and Chemale, F.: Release of mineral-bound water prior to subduction tied to shallow
842   seismogenic slip off Sumatra. Science, 356(6340), 841-844. 2017.

843   Jiang, M., Klaver, J., Schmatz, J. and Urai, J.L.: Nanoscale porosity analysis in geological materials. Acta
844   Stereologica, 2015.

845   Kameda, A., Dvorkin, J., Keehm, Y., Nur, A. and Bosl, W.: Permeability-porosity transforms from small sandstone

846   fragments. Geophysics, 71(1), N11-N19, https://doi.org/10.1190/1.2159054, 2006.

847   Karaborni, S., Smit, B., Heidug, W., Urai, J. and Van Oort, E.: The swelling of clays: molecular simulations of

848   the hydration of montmorillonite. Science, 271(5252), 1102-1104, DOI: 10.1126/science.271.5252.1102, 1996.

849   Klaver, J., Desbois, G., Littke, R. and Urai, J.L.: BIB-SEM characterization of pore space morphology and

850   distribution in postmature to overmature samples from the Haynesville and Bossier Shales. Marine and petroleum

851   Geology, 59, 451-466, https://doi.org/10.1016/j.marpetgeo.2014.09.020, 2015.

852   Klaver, J., Desbois, G., Littke, R. and Urai, J.L.: BIB-SEM pore characterization of mature and post mature

853   Posidonia Shale samples from the Hils area, Germany. International Journal of Coal Geology, 158, 78-89,

854   https://doi.org/10.1016/j.coal.2016.03.003, 2016.

855   Klaver, J., Desbois, G., Urai, J.L. and Littke, R.: BIB-SEM study of the pore space morphology in early mature

856   Posidonia Shale from the Hils area, Germany. International Journal of Coal Geology, 103, 12-25.

857   https://doi.org/10.1016/j.coal.2012.06.012, 2012.

858   Kuila, U. and Prasad, M.: Specific surface area and pore-size distribution in clays and shales. Geophysical

859   Prospecting, 61(2-Rock Physics for Reservoir Exploration, Characterisation and Monitoring), pp.341-362,

860   https://doi.org/10.1111/1365-2478.12028, 2013.

861   Lander, R. H. and Walderhaug, O. W.: Predicting porosity through simulating sandstone compaction and quartz

862   cementation.   American   Association   of   Petroleum   Geologists   Bulletin   83:   433-449,

863   https://doi.org/10.1306/00AA9BC4-1730-11D7-8645000102C1865D, 1999.

864   Lander, R. H., Larese, R. H. Larese and Bonnell, L. M.: Toward more accurate quartz cement models: The

865   importance of euhedral versus noneuhedral growth rates. American Association Petroleum Geologists Bulletin 92:

866   1537-1563. https://doi.org/10.1306/07160808037, 2008.

867   Laurich, B., Urai, J.L., Desbois, G., Vollmer, C. and Nussbaum, C.: Microstructural evolution of an incipient fault

868   zone in Opalinus Clay: Insights from an optical and electron microscopic study of ion-beam polished samples from

869   the Main Fault in the Mt-Terri Underground Research Laboratory. Journal of Structural Geology, 67, 107-128.

870   https://doi.org/10.1016/j.jsg.2014.07.014, 2014.

871   Lay, T., Kanamori, H., Ammon, C. J., Nettles, M., Ward, S.N., Aster, R.C., Beck, S.L., Bilek, S.L., Brudzinski,

872   M.R., Butler, R. and DeShon, H.R.: The great Sumatra-Andaman earthquake of 26 Ddecember

873   2004. Sscience, 308(5725), pp.1127-1133, DOI: 10.1126/science.1112250, 2005.

874   Lazar, O.R., Bohacs, K.M., Macquaker, J.H., Schieber, J. and Demko, T.M.: Capturing key attributes of fine-

875   grained sedimentary rocks in outcrops, cores, and thin sections: nomenclature and description guidelines. Journal

876   of Sedimentary Research, 85(3), pp.230-246, https://doi.org/10.2110/jsr.2015.11, 2015.

877 Lundegard, P. D.: Sandstone porosity loss--a 'big picture' view of the importance of compaction. Journal of
878 Sedimentary Petrology 62: 250-260, https://doi.org/10.1306/D42678D4-2B26-11D7-8648000102C1865D, 1992.

879 March, A.: Mathematical theory of the Korngestah control for affine deformation. Journal of Crystallography-
880 Crystalline Materials , 81 (1-6), 285-297, doi.org/10.1524/zkri.1932.81.1.285, 1932.

881 McNeill, L.C., Dugan, B. and Petronotis, K.E., Backman, J., Bourlange, S., Chemale, F., Chen, W., Colson, T.A.,
882 Frederik, M.C.G., Guèrin, G., Hamahashi, M., Henstock, T., House, B.M., Hüpers, A., Jeppson, T.N., Kachovich,
883 S., Kenigsberg, A.R., Kuranaga, M., Kutterolf, S., Milliken, K.L., Mitchison, F.L., Mukoyoshi, H., Nair, N.,
884 Owari, S., Pickering, K.T., Pouderoux, H.F.A., Yehua, S., Song, I., Torres, M.E., Vannucchi, P., Vrolijk, P.J.,
885 Yang, T., and Zhao, X.: Sumatra Subduction Zone. Proceedings of the International Ocean Discovery
886 Program, 362, https://doi.org/10.14379/iodp.proc.362.102.2017, 2017a.

887 McNeill, L.C., Dugan, B. and Petronotis, K.E., Backman, J., Bourlange, S., Chemale, F., Chen, W., Colson, T.A.,
888 Frederik, M.C.G., Guèrin, G., Hamahashi, M., Henstock, T., House, B.M., Hüpers, A., Jeppson, T.N., Kachovich,
889 S., Kenigsberg, A.R., Kuranaga, M., Kutterolf, S., Milliken, K.L., Mitchison, F.L., Mukoyoshi, H., Nair, N.,
890 Owari, S., Pickering, K.T., Pouderoux, H.F.A., Yehua, S., Song, I., Torres, M.E., Vannucchi, P., Vrolijk, P.J.,
891 Yang, T., and Zhao, X.: Sumatra Subduction Zone. Proceedings of the International Ocean Discovery
892 Program, 362, (Supplementary material), https://doi.org/10.14379/iodp.proc.362supp.2017, 2017b.

893 Meade, R.H.: Removal of water and rearrangement of particles during the compaction of clayey sediments. US
894 Government Printing Office, 1964.

895 Mesri, G. and Olson, R.E.: Mechanisms controlling the permeability of clays. Clays and Clay minerals, 19(3),
896 151-158, 1971.

897 Milliken, K. L.: A compositional classification for grain assemblages in fine-grained sediments and sedimentary
898 rocks. Journal of Sedimentary Research 84: 1185-1199, https://doi.org/10.2110/jsr.2014.92, 2008.

899 Milliken, K. L.: A compositional classification for grain assemblages in fine-grained sediments and sedimentary
900 rocks. Journal of Sedimentary Research 84: 1185-1199, https://doi.org/10.2110/jsr.2014.92, 2014.

901 Milliken K. L.: Compactional and mass-balance constraints inferred from the volume of quartz cementation in
902 mudrocks. Mudstone Diagenesis: New Research Perspectives for Shale Hydrocarbon Reservoirs, Seals, and
903 Source Rocks. AAPG. 120: 33-48, DOI: 10.1306/13672209M121252, 2019.

904 Milliken, K. L. and Curtis, M. E.: Imaging pores in sedimentary rocks: Foundation of porosity prediction. Marine
905 and Petroleum Geology 73,: 590-608, https://doi.org/10.1016/j.marpetgeo.2016.03.020, 2016.

906 Milliken, K. L. and Day-Stirrat R. J.: Cementation in mudrocks: Brief review with examples from cratonic basin
907 mudrocks. Memoir. J.-Y. Chatellier. Tulsa, Oklahoma, USA, AAPG, https://doi.org/10.1306/13401729H55252,
908 2013.

909 Milliken, K. L. and Olson, T.: Silica diagenesis, porosity evolution, and mechanical behavior in siliceous
910 mudstones, Mowry Shale Cretaceous, Rocky Mountains, U.S.A. Journal of Sedimentary Research 87: 366-387,
911 .https://doi.org/10.2110/jsr.2017.24, 2017.

912 Milliken, K. L., Rudnicki, M., Awwiller, D. N. and Zhang, T.: Organic matter-hosted pore system, Marcellus
913 Formation Devonian, Pennsylvania, USA. AAPG Bulletin 97: 177-200, https://doi.org/10.1306/07231212048,
914 2013.

915 Milliken, K.L. and Reed, R.M.: Multiple causes of diagenetic fabric anisotropy in weakly consolidated mud,
916 Nankai accretionary prism, IODP Expedition 316. Journal of Structural Geology, 32(12), 1887-1898,
917 doi.org/10.1016/j.jsg.2010.03.008, 2010.

918 Milliken, K. L., Esch, W. L., Reed, R. M. and Zhang. T.: Grain assemblages and strong diagenetic overprinting
919 in siliceous mudrocks, Barnett Shale Mississippian, Fort Worth Basin, Texas, U.S.A. AAPG Bulletin 96: 1553-
920 1578, https://doi.org/10.1306/12011111129, 2012.

921 Mitchell, J.K.: The fabric of natural clays and its relation to engineering properties. In Highway Research Board
922 Proceedings, 35, 1956.

923 Moeremans, R.E. and Singh, S.C.: Fore-arc basin deformation in the Andaman-Nicobar segment of the Sumatra-
924 Andaman subduction zone: Insight from high-resolution seismic reflection data, Tectonics, 34(8), 1736-1750,
925 doi.org/10.1002/2015TC003901, 2015.

926 Mondol, N.H., Bjørlykke, K., Jahren, J. and Høeg, K.: Experimental mechanical compaction of clay mineral
927 aggregates—Changes in physical properties of mudstones during burial. Marine and petroleum geology, 24(5),
928 289-311, https://doi.org/10.1016/j.marpetgeo.2007.03.006, 2007.

929 Morgenstern, N.R. and Tchalenko, J.S.: Microstructural observations on shear zones from slips in natural clays,
930 1967.

931 Nakano, R.: On weathering and change of properties of tertiary mudstone related to landslide. Soils and
932 Foundations, 7(1), 1-14, https://doi.org/10.3208/sandf1960.7.1, 1967.

933 Neagu, R.C., Cartwright, J. and Davies, R.: Measurement of diagenetic compaction strain from quantitative
934 analysis of fault plane dip. Journal of Structural Geology, 32(5), 641-655,
935 https://doi.org/10.1016/j.jsg.2010.03.010, 2010.

936 Nole, M., Daigle, H., Milliken, K.L. and Prodanović, M.: A method for estimating microporosity of fine-grained
937 sediments and sedimentary rocks via scanning electron microscope image analysis. Sedimentology, 63(6), 1507-
938 1521, https://doi.org/10.1111/sed.12271, 2016.

939 Nollet, S., Hilgers, C. and Urai, J.: Sealing of fluid pathways in overpressure cells: a case study from the
940 Buntsandstein in the Lower Saxony Basin (NW Germany). International Journal of Earth Sciences, 94(5), 1039-
941 1055, https://doi.org/10.1007/s00531-005-0492-1, 2005.

942 Oelker, A.: Deformation properties of Boom Clay: Implementation of a multi-scale concept. Dissertation,
943 Rheinisch-Westfälische Technische Hochschule Aachen, DOI: 10.18154/RWTH-2019-09913, 2019.

944 Oertel, G. and Curtis, C.D.: Clay-ironstone concretion preserving fabrics due to progressive
945 compaction. Geological Society of America Bulletin, 83(9), 2597-2606, https://doi.org/10.1130/0016-
946 7606(1972)83[2597:CCPFDT]2.0.CO;2, 1972.

947 Paxton, S. T., J. O. Szabo, J. M. Adjukiewicz and R. E. Klimentidis.: Construction of an intergranular volume
948 compaction curve for evaluating and predicting compaction and porosity loss in rigid-grain sandstone reservoirs.
949 American Association of Petroleum Geologists Bulletin 86: 2047-2067, https://doi.org/10.1306/61EEDDFA-
950 173E-11D7-8645000102C1865D, 2002.

951 Pickering, K.T., Carter, A., Andò, S., Garzanti, E., Limonta, M., Vezzoli, G. and Milliken, K.L.: 2020. Deciphering
952 relationships between the Nicobar and Bengal submarine fans, Indian Ocean. Earth and Planetary Science
953 Letters, 544, 116329, https://doi.org/10.1016/j.epsl.2020.116329, 2020.

954 Pommer, M. E. and Milliken, K. L.: Pore types and pore-size distributions across thermal maturity, Eagle Ford
955 Formation, South Texas. AAPG Bulletin 99: 1713-1744, https://doi.org/10.1306/03051514151, 2015.

956 Prawirodirdjo, L., Bocl, Y., McCaffrey, R., Genrich, J., Calais, E., Stevens, C., Puntodewo, S.S.O., Subarya, C.,
957 Rais, J., Zwick, P. and Fauzi, R.M.: Geodetic observations of interseismic strain segmentation at the Sumatra
958 subduction zone. Geophysical research letters, 24(21), 2601-2604, https://doi.org/10.1029/97GL52691, 1997.

959 Rieke, H.H. and Chilingarian, G.V.: Compaction of argillaceous sediments. Elsevier, 1974.

960 Rosenberger, K., Underwood, M.B., Vrolijk, P. and Haines, S.: Data report: clay mineral assemblages in
961 hemipelagic sediments entering the Sumatra subduction zone, IODP Sites U1480 and U1481, Expedition
962 362. Expedition, 362, 1. 2020.

963 Samsudin, M.S.F., Ariff, Z.M. and Ariffin, A.: Deformation behavior of open-cell dry natural rubber foam: Effect
964 of different concentration of blowing agent and compression strain rate. In AIP Conference Proceedings, 1835,
965 No. 1, 020007, AIP Publishing LLC, 2017.

966 Schmatz, J., Klaver, J., Jiang, M. and Urai, J.L.: Nanoscale morphology of brine/oil/mineral contacts in connected
967 pores of carbonate reservoirs: Insights on wettability from Cryo-BIB-SEM. SPE Journal, 22(05), 1374-1384,
968 https://doi.org/10.2118/180049-PA, 2017.

969 Schneider, J., Flemings, P.B., Day-Stirrat, R.J. and Germaine, J.T.: Insights into pore-scale controls on mudstone
970 permeability through resedimentation experiments. Geology, 39(11), 1011-1014,
971 https://doi.org/10.1130/G32475.1 , 2011.

972 Sintubin, M.: Clay fabrics in relation to the burial history of shales. Sedimentology, 41(6), 1161-1169,
973 https://doi.org/10.1130/G32475.1, 1994.

974 Terzaghi, K. and Peck, R.B.: Soil Mechanics. Engineering Practice. John Wiley and Sons, Inc., New York, 1948.

975 Torres, M. E., Milliken, K. L., A. Hüpers, J. H. Kim, S. G. Lee: Authigenic clays versus carbonate formation as
976 products of marine silicate weathering in the input sequence to the Sumatra Subduction Zone, Gechemistry,
977 Geophysics Geosystems, 23 (4), https://doi.org/10.1029/2022GC010338, 2022.

978 Ukar, E. and Cloos, M.: Cataclastic deformation and metasomatism in the subduction zone of mafic blocks-in-
979 mélange, San Simeon, California, Lithos, 346, 105116, https://doi.org/10.1016/j.lithos.2019.06.018, 2019.

980 Underwood, M. B., N. Lawler, and K. McNamara.: Data report: standard mineral mixtures, normalization factors,
981 and determination of error for quantitative X-ray diffraction analyses of bulk powders and clay-sized mineral
982 assemblages. Proceedings of the International Ocean Discovery Program, 372,
983 doi.org/10.14379/iodp.proc.372B375.201.2020, 2020.

984 Vasseur, G., Djeran-Maigre, I., Grunberger, D., Rousset, G., Tessier, D. and Velde, B.: Evolution of structural and
985 physical parameters of clays during experimental compaction, Marine and petroleum geology, 12(8), pp.941-954,
986 https://doi.org/10.1016/0264-8172(95)98857-2, 1995.

987 Velde, B.: Compaction trends of clay-rich deep sea sediments, Marine Geology 133(3-4): 193-201,
988 https://doi.org/10.1016/0025-3227(96)00020-5, 1996.

989 Vrolijk, P.: On the mechanical role of smectite in subduction zones. Geology, 18(8), pp.703-707,
990 https://doi.org/10.1130/0091-7613(1990)018<0703:OTMROS>2.3.CO;2, 1990.

991 Wang, X., Jiang, Z., Jiang, S., Chang, J., Zhu, L., Li, X. and Li, J.: Full-scale pore structure and fractal dimension
992 of the Longmaxi shale from the Southern Sichuan Basin: Investigations using FE-SEM, gas adsorption and
993 mercury intrusion porosimetry. Minerals, 9(9), p.543, https://doi.org/10.3390/min9090543, 2019.

994 Worden, R.H., Charpentier, D., Fisher, Q.J. and Aplin, A.C.: Fabric development and the smectite to illite
995 transition in Upper Cretaceous mudstones from the North Sea: an image analysis approach. Geological Society,
996 London, Special Publications, 249(1), 103-114, doi.org/10.1144/GSL.SP.2005.249.01.0, 2005.

997 Yagiz, S.: Overview of classification and engineering properties of shales for design considerations.
998 In Construction and Materials Issues 2001, 156-165, 2001.

999 Zakaria, Z., Mohamad Ariff, Z. and Abu Bakar, A.: Monitoring deformation mechanism of foam cells in

1000 polyethylene foams via optical microscopy: Effect of density and microstructure. Journal of Cellular

1001 Plastics, 54(6), 957-976, https://doi.org/10.1177/0021955X18795035, 2018.

1002 Zhou, J., Shrotriya, P. and Soboyejo, W.O.: Mechanisms and mechanics of compressive deformation in open-cell

1003 Al foams. Mechanics of Materials, 36(8), 781-797, https://doi.org/10.1016/j.mechmat.2003.05.004,. 2004.

1004
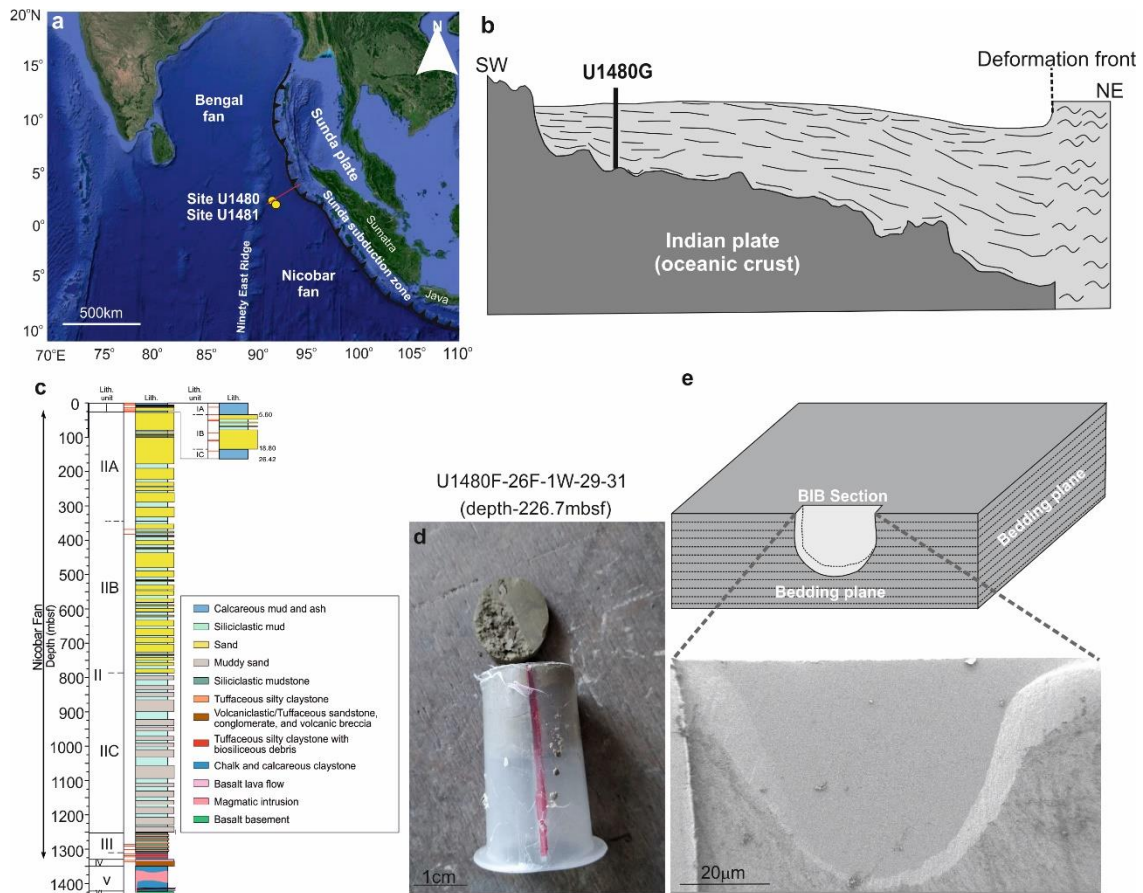
1005

1006 **Fig.1:** (a) Satellite image of Sumatra subduction zone and location of U1480 and U1481 drilling sites (created

1007 from © Google Maps). (b) Schematic diagram showing location of primary drilling site and deepest drill hole

1008 (Hole G) at site U1480 in sectional view (adapted from seismic profile from SW to NE after Hüpers et al., 2017).

1009 Location and extension of the seismic profile is represented by red line in (a). (c) Lithostratigraphic units

1010 encountered at Site U1480 (adapted after McNeill et al., 2017a). (d) Representative tube sample received from

1011 IODP repository, Japan. Red-colored line on tube surface represents notch used to denote orientation of samples

1012 collected from drill core. (e) Representative BIB cross-section polished perpendicular to bedding plane.

1013
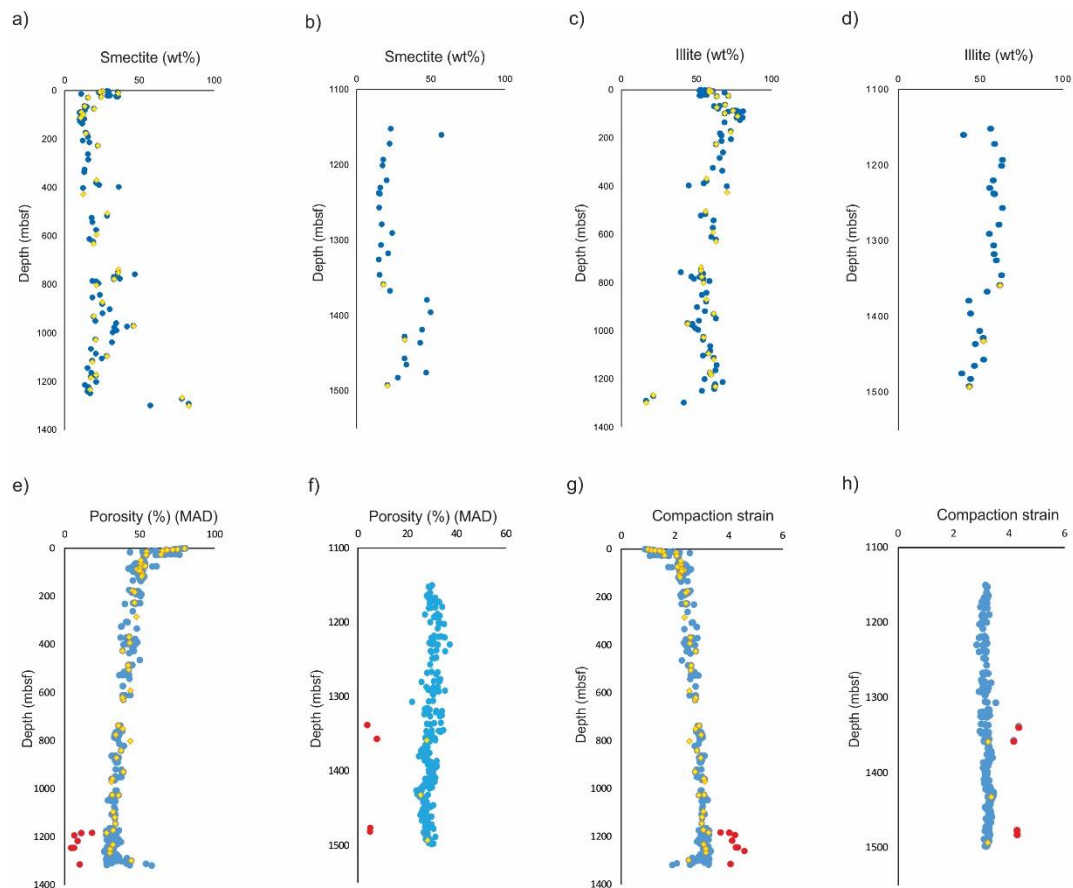
1014 **Fig.2:** Depth profiles of smectite content (wt%; clay fraction) for Sites U1480 (a) and U1481 (b) (blue symbol).
1015 Depth profiles of illite content (wt%; clay fraction) for Sites U1480 (a) and U1481 (b) (blue symbol). Yellow
1016 symbols indicate samples analyzed by SEM imaging. (e) and (f) Shipboard MAD (Moisture and density) porosity
1017 profiles for mudstone samples recovered from Sites U1480 and U1481 (blue symbol). (g) and (h) Calculated
1018 compaction strain profiles for Sites U1480 and U1481 (blue symbols). Red-colored points are cemented
1019 (concretion) samples. Clay mineralogy data plotted from Rosenberger et al. (2020), and MAD data extracted from
1020 McNeill et al. (2017b).

1021

1022

1023

1024

1025

1026

1027
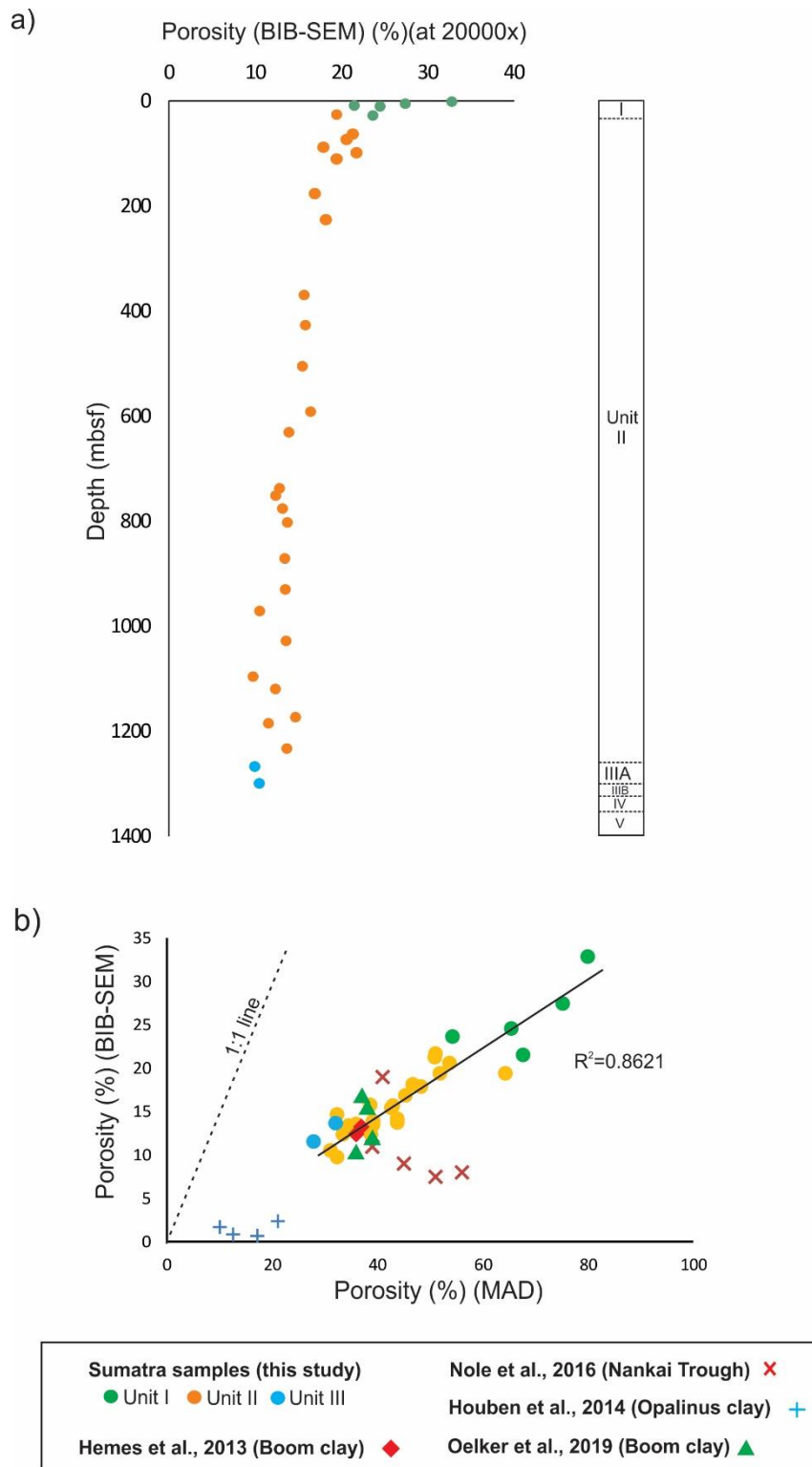
1028

1029   **Fig.3:** Porosity data for Units I (green dots), II (orange dots), and IIIA (blue dots). (a) BIB-SEM porosity - depth

1030   plot, (b) BIB-SEM porosity vs MAD porosity. Note: linear relationship that intersects origin. Data reported by

1031   Hemes et al. (2013); Houben et al. (2014); and Oelker et al. (2019) follow similar trend. However, data estimated

1032   from Nole et al. (2016) deviates from trend.
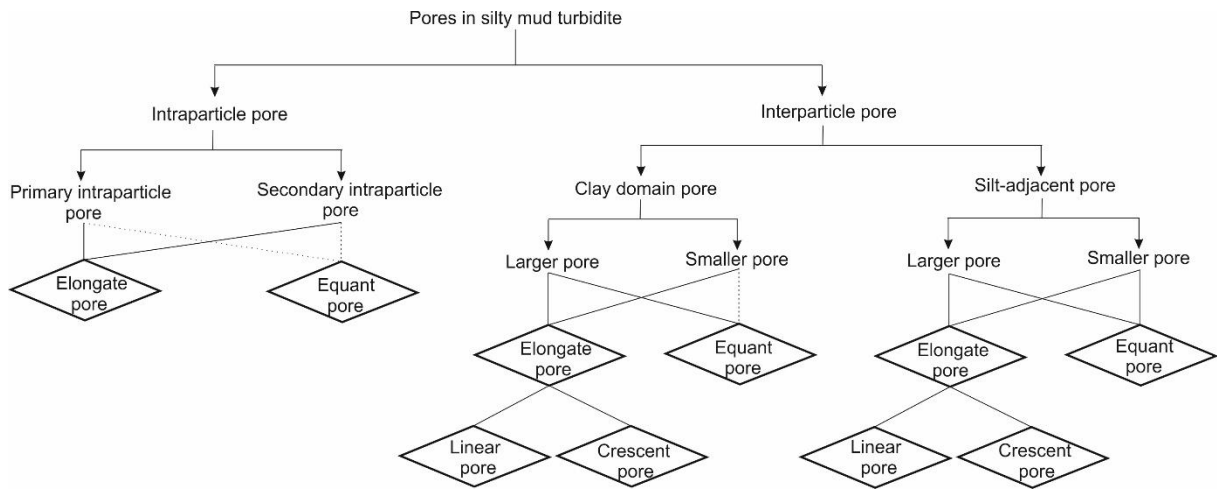
 Fig.4: Classification scheme adopted to demonstrate pore reduction mechanics with increasing compactional

 strain. Dashed lines indicate rare pore types.

1051
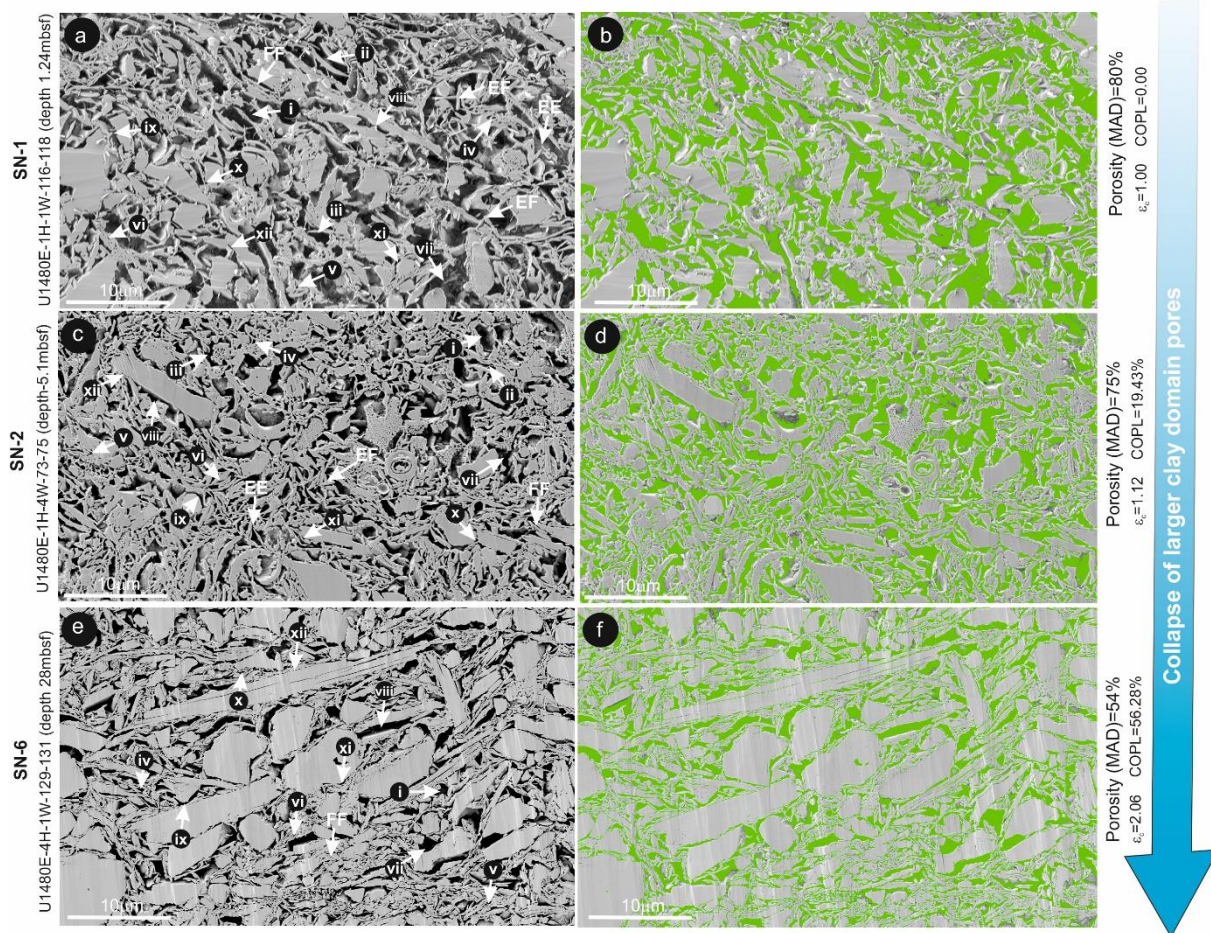
Fig.5: Microstructural overview (BIB-SEM) of samples SN-1 (a and b), SN-2 (c and d), and SN-6 (e and f). Green color represents segmented pores of the corresponding microstructure of sample.i = Equant large clay domain pores, ii = elongated large clay domain pores, iii = Crescent-shaped large clay domain pores, iv = equant small clay domain pores, v = Crescent-shaped small clay domain pores, vi = elongated small clay domain pores, vii = Equant large silt-adjacent pores, viii = elongated large silt-adjacent pores, ix = Crescent-shaped large silt-adjacent pores, x =equant small silt-adjacent pores, xi = Crescent-shaped small silt-adjacent pores, xii = elongated small silt-adjacent pores. EE= Edge to edge contact, EF=Edge to face contact, and FF=Face to face contact.

1059

1060

1061

1062

1063

1064
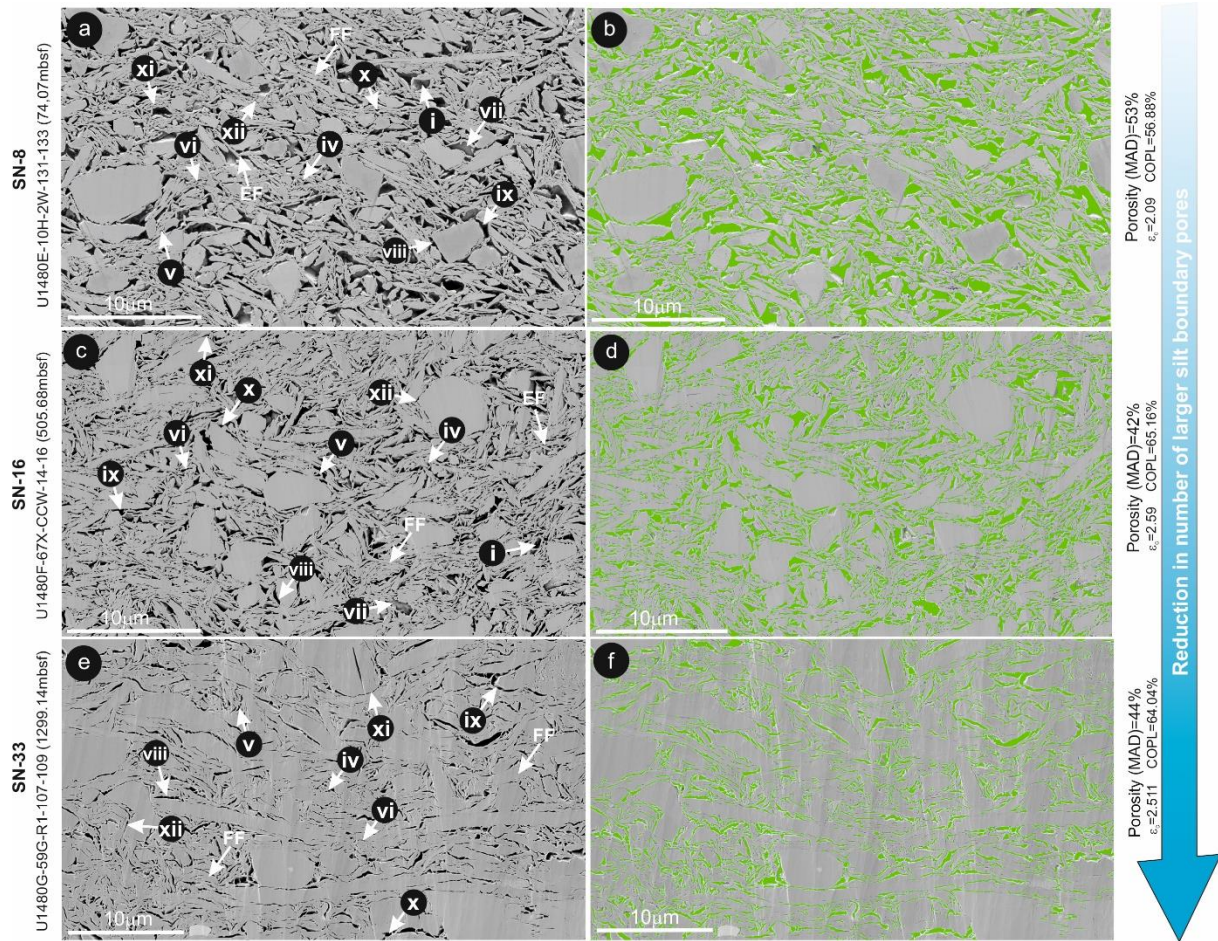
1065

Fig.6: Microstructural overview (BIB-SEM) of samples SN-8 (a and b), SN-16 (c and d), and SN-33 (e and f). Green color represents segmented pores of the corresponding microstructure of sample. i = Equant large clay domain pores, ii = elongated large clay domain pores, iii = Crescent-shaped large clay domain pores, iv = equant small clay domain pores, v = Crescent-shaped small clay domain pores, vi = elongated small clay domain pores, vii = Equant large silt-adjacent pores, viii = elongated large silt-adjacent pores, ix = Crescent-shaped large silt-adjacent pores, x =equant small silt-adjacent pores, xi = Crescent-shaped small silt-adjacent pores, xii = elongated small silt-adjacent pores. FF= Face to face contact, EF= Edge to face contact.

1073

1074

1075

1076

1077

1078

1079
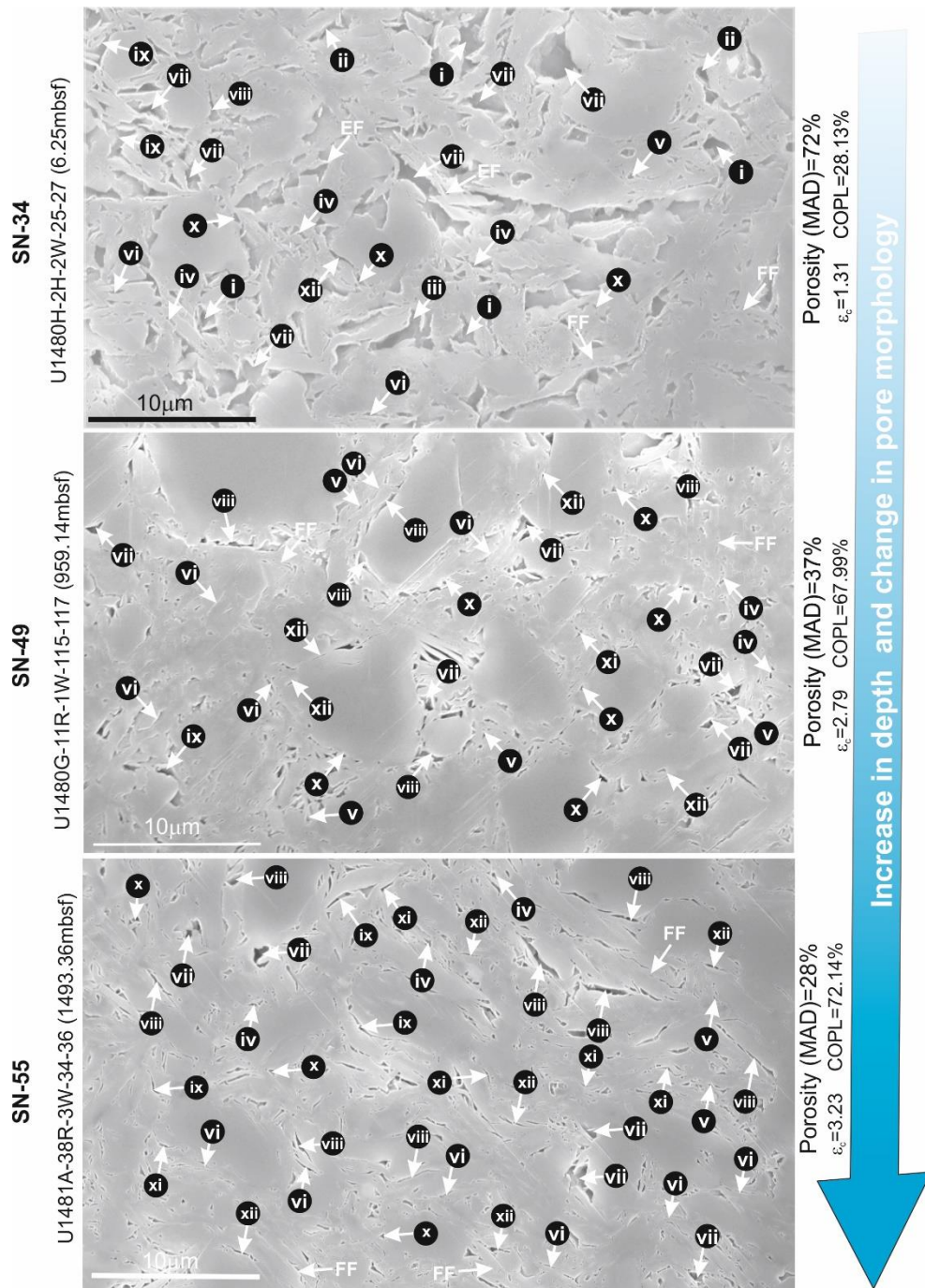
1080

1081 **Fig.7:** Microstructural overview (Field Emission SEM) of samples SN-34, SN-49, and SN-55. i = Equant large
1082 clay domain pores, ii =elongated large clay domain pores, iii = Crescent-shaped large clay domain pores, iv =
1083 equant small clay domain pores, v = Crescent-shaped small clay domain pores, vi = elongated small clay domain
1084 pores, vii = Equant large silt-adjacent pores, viii = elongated large silt-adjacent pores, ix = Crescent-shaped large
1085 silt-adjacent pores, x =equant small silt-adjacent pores, xi = Crescent-shaped small silt-adjacent pores, xii =
1086 elongated small silt-adjacent pores. FF= Face to face contact, EF= Edge to face contact.
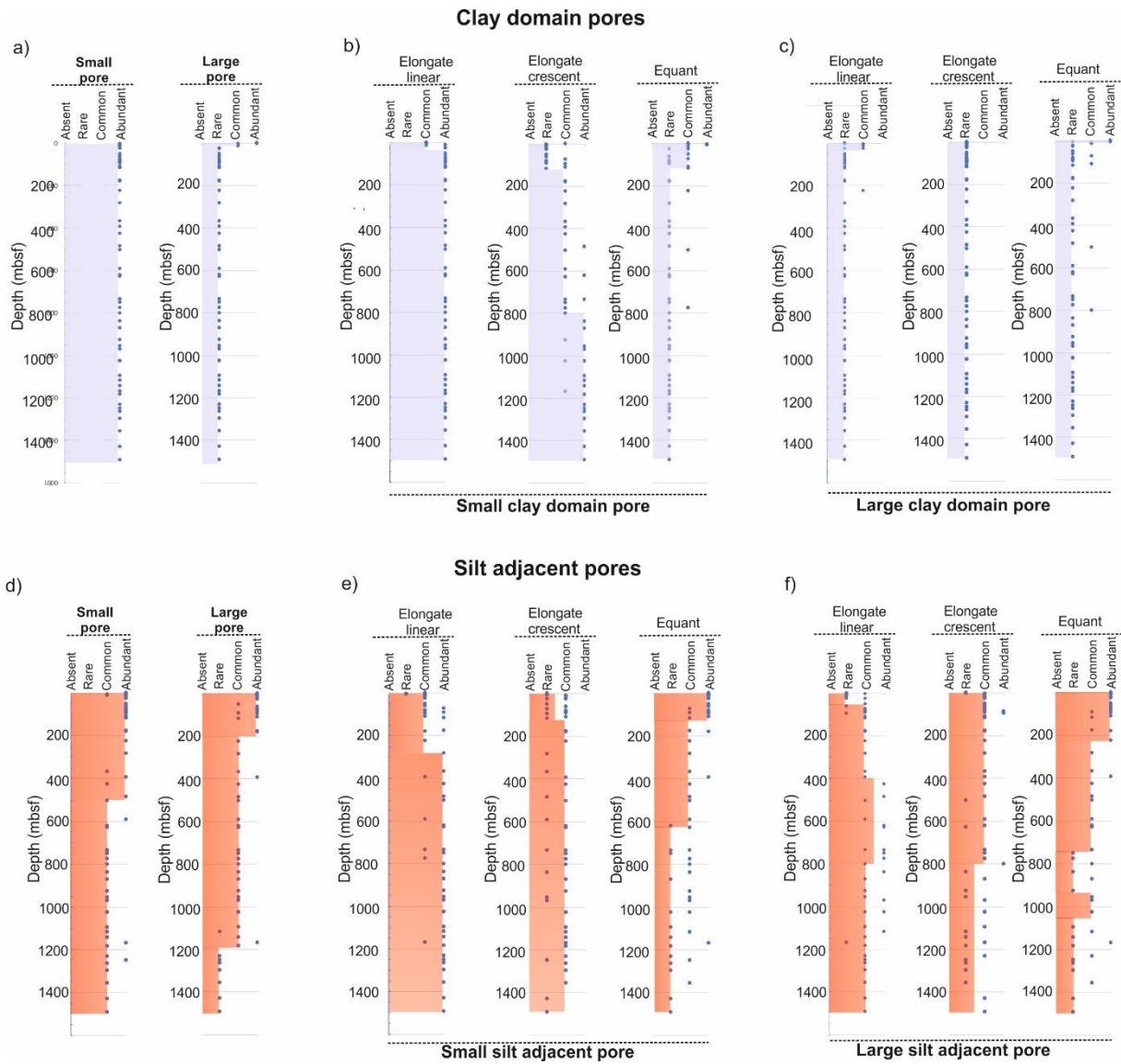
Fig.8: Pore type summary for clay domain (a-c) and silt-adjacent (d-f) pore types. (a) abundance of small and large clay domain pores; (b) and (c) depth progression of small and large clay domain pore morphologies; (d) abundance of small and large silt-adjacent pores; (e) and (f) depth progression of small and large clay domain pore morphologies. Abundant = >25% pores, common = 2%-25% pores, rare = 0-2% pores, absent = not observed.
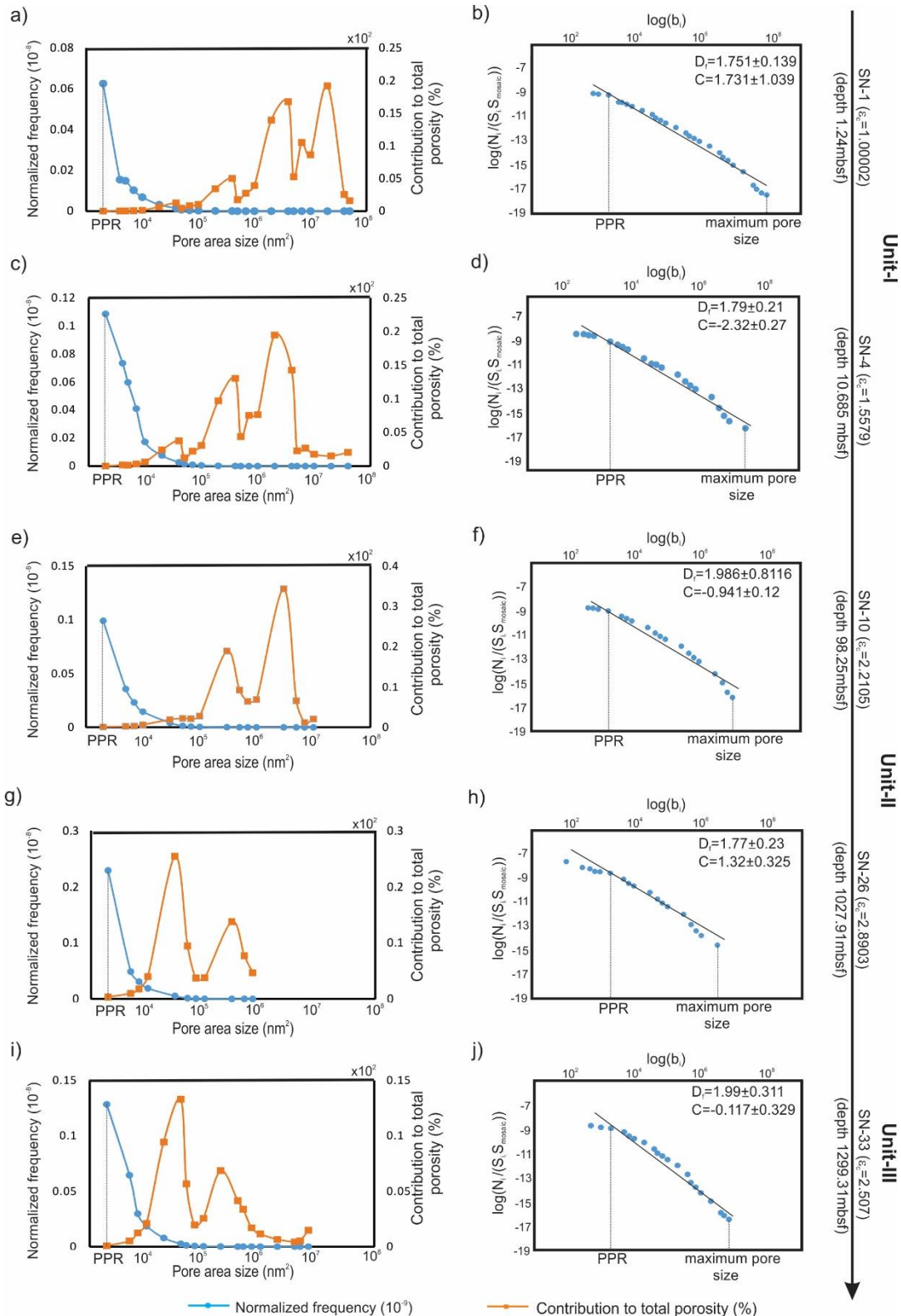
Fig.9: Pore size distribution defined by pore area. Left column: normalized frequency (blue) and contribution to total porosity (orange). Right column: pore size-frequency log-log distribution. Power-law between PPR and maximum pore size interpreted as black line with corresponding regression parameters. Sample number, depth, and compactional strain defined along right side of diagram

1103
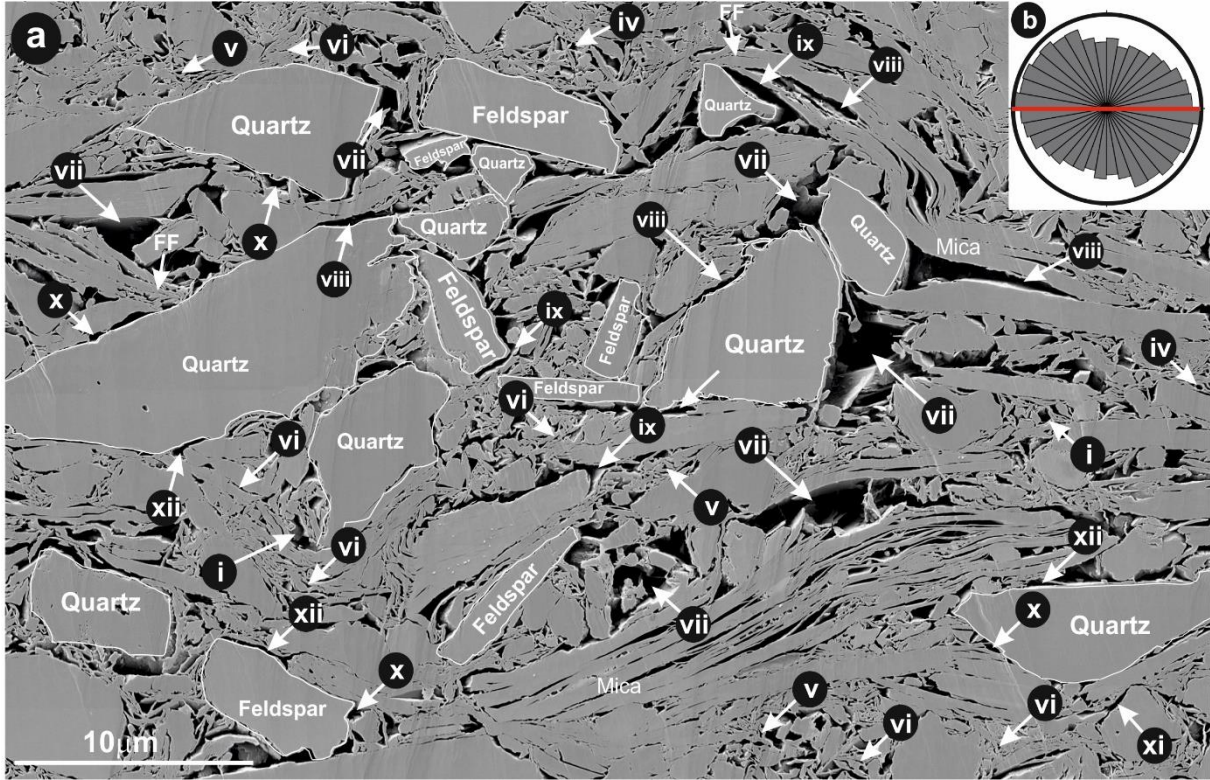
Fig.10: Silt-rich sample (SN-29; 1173 mbsf) (a) i = Equant large clay domain pores, ii =elongated large clay domain pores, iii = Crescent-shaped large clay domain pores, iv = equant small clay domain pores, v = Crescent-shaped small clay domain pores, vi = elongated small clay domain pores, vii = Equant large silt-adjacent pores, viii = elongated large silt-adjacent pores, ix = Crescent-shaped large silt-adjacent pores, x =equant small silt-adjacent pores, xi = Crescent-shaped small silt-adjacent pores, xii = elongated small silt-adjacent pores.(b) Rose diagram of long axes of pores (bedding = red line). FF= face to face contact of clay particles.

1120
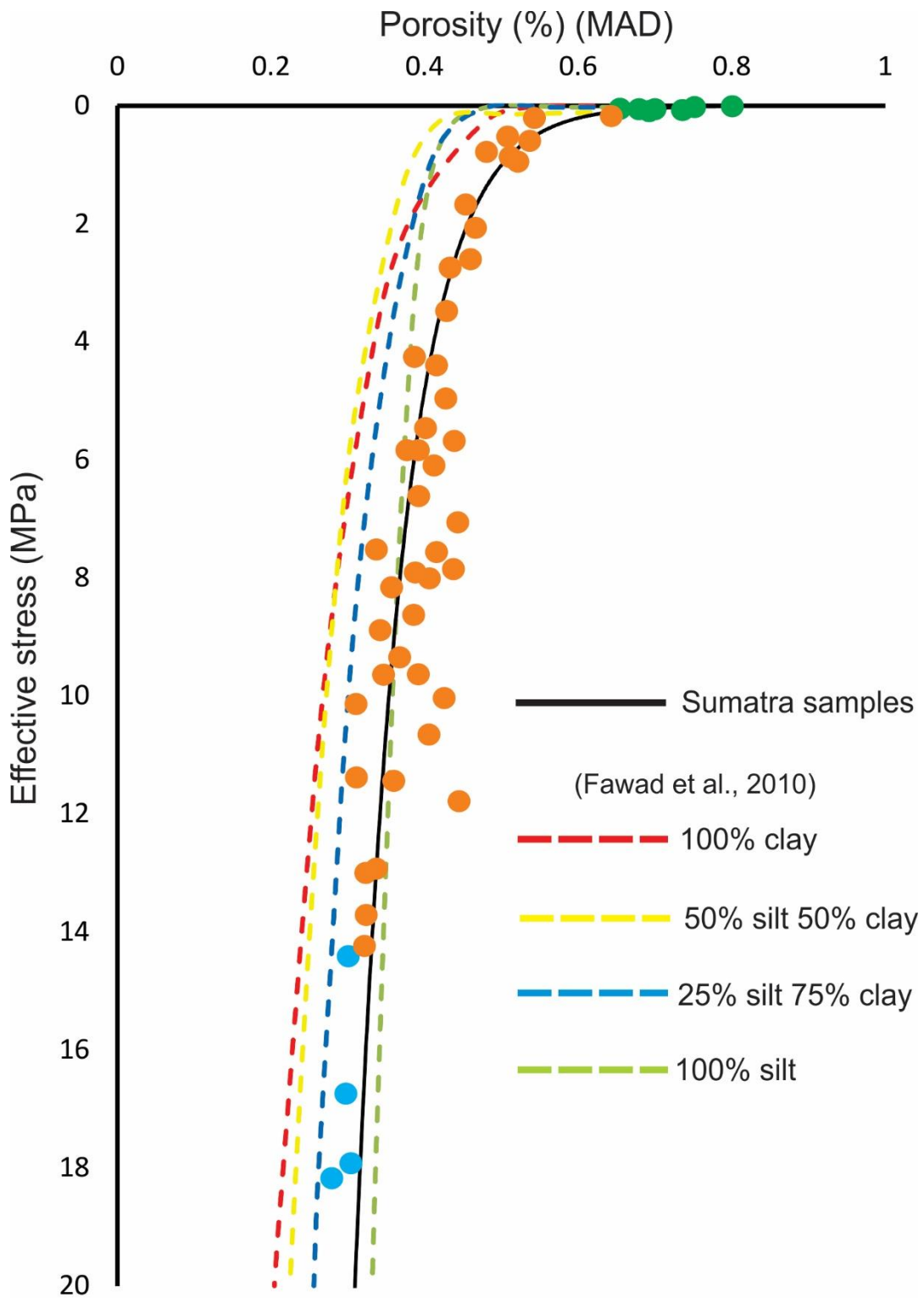
1121

1122 **Fig.11:** Effective stress vs porosity (MAD) for experimental mixtures of clay and silt (dashed lines; Fawad et al.,
1123 2010) compared with Sumatra data (Unit 1 = green; Unit II = orange; Unit III = blue). Solid black solid line is a
1124 best-fit data regression for Sumatra samples.
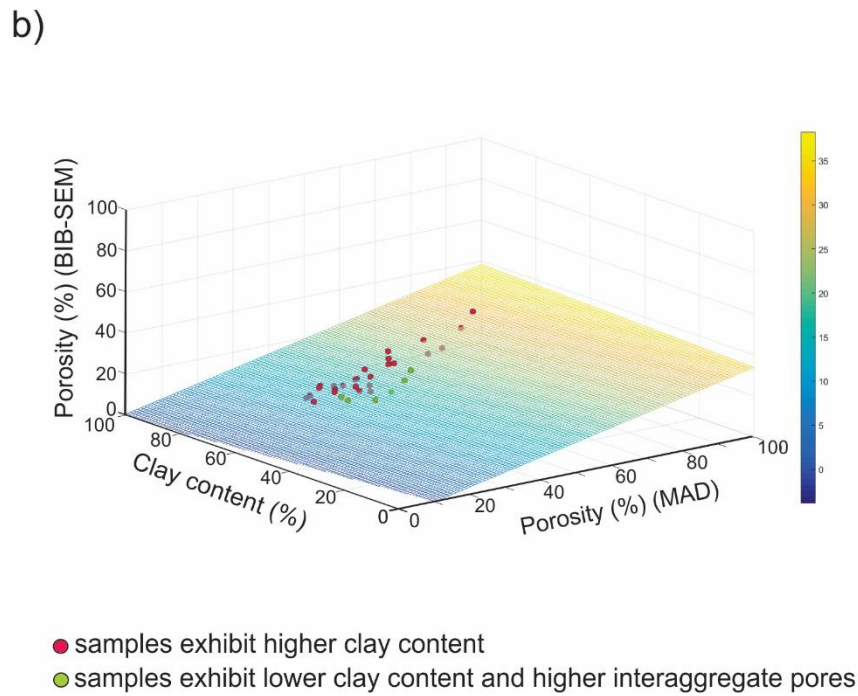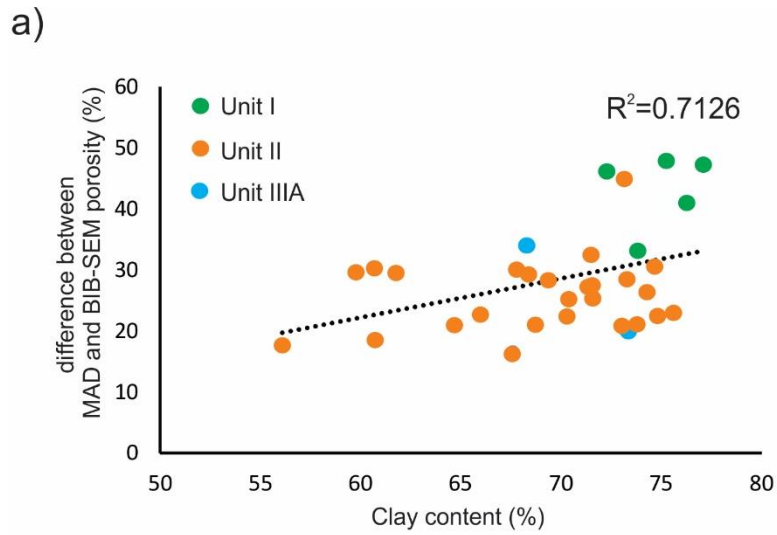
1125

Fig.12: (a) Clay content vs difference between MAD and BIB-SEM porosity. Green, orange and blue colored symbols represent the samples from Unit-I, II and III respectively. (b) Multivariate regression analysis using three parameters: BIB-SEM porosity, clay content, and MAD porosity (33 samples).

1129

1130

1131
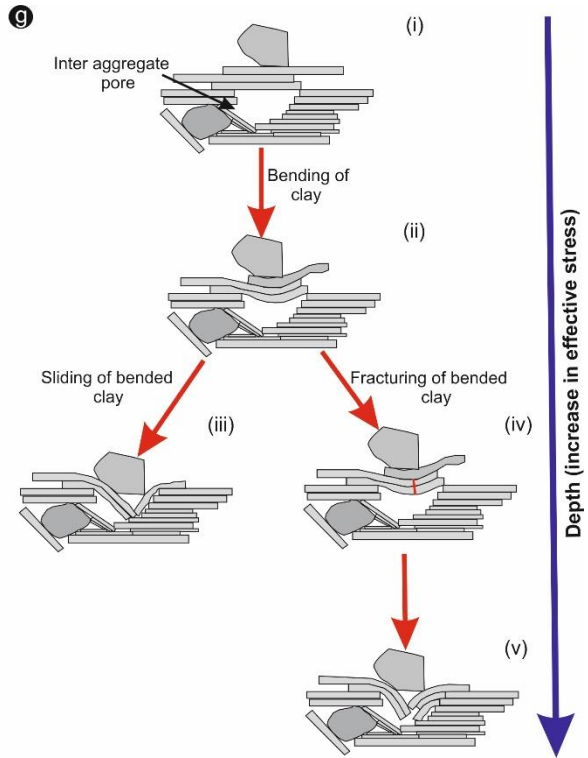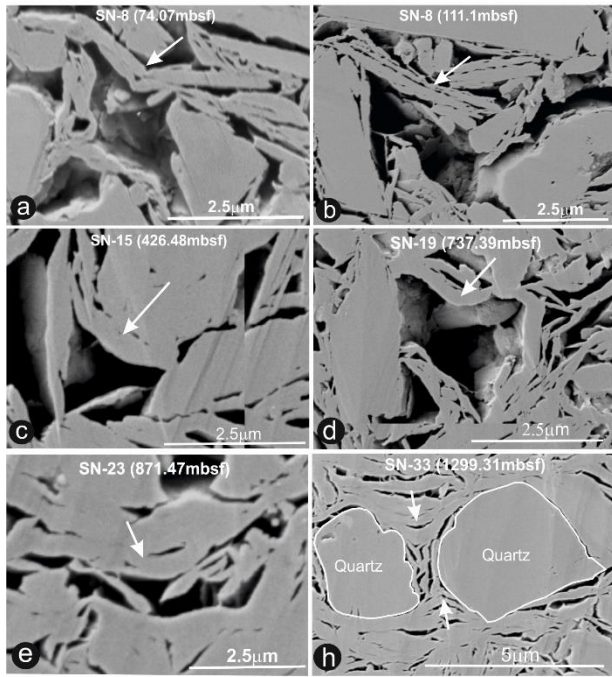
1132

Fig.13: a-f: examples of bent clay particles on top of silt-adjacent larger pores; sample ID and depth labelled on photos. (g) Micromechanical model for collapse of large silt-adjacent pores.

1133

1134

1135

1136

1137

1138

1139

1140

1141

1142

1143
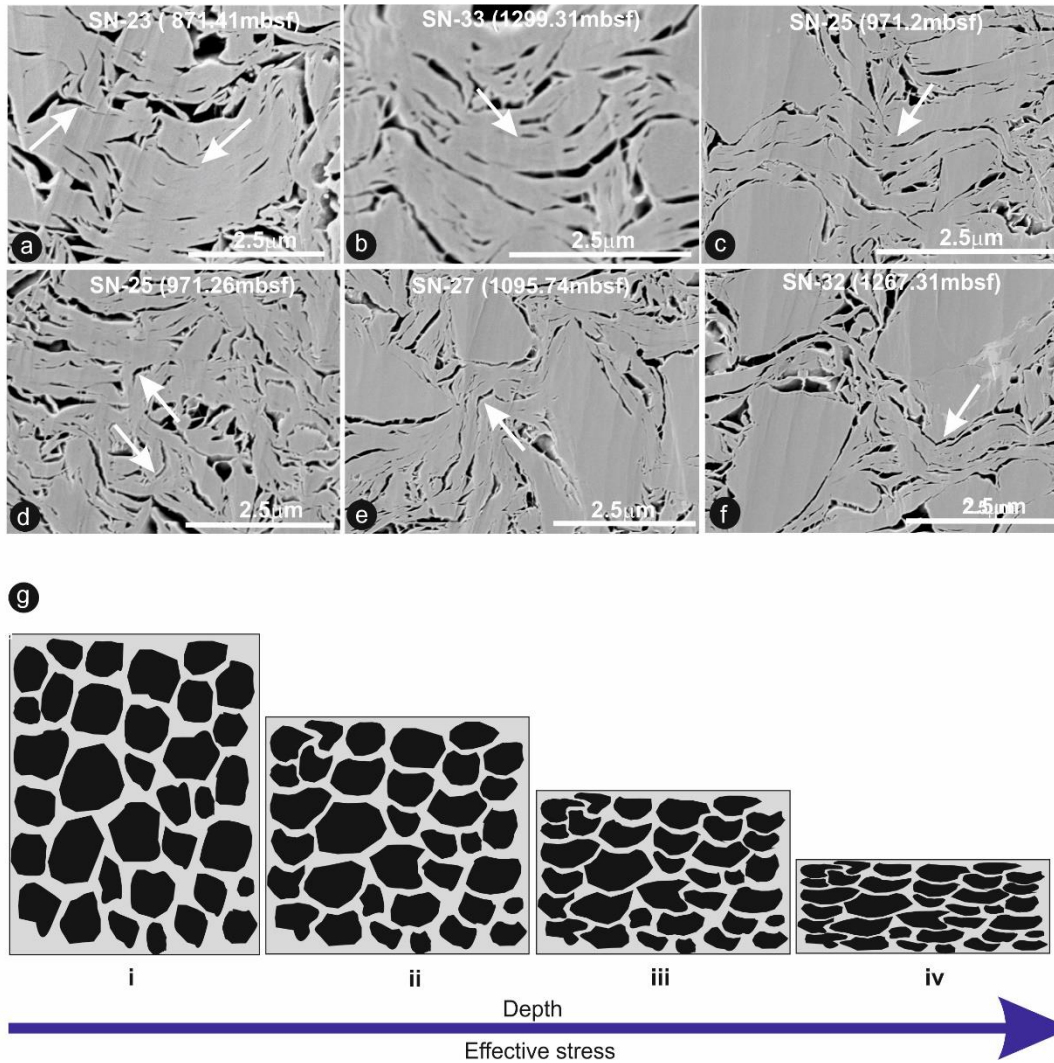
Fig.14: a-f: examples of clay aggregate bending (white arrows). (g) Conceptual diagram tracing porosity reduction and increase in preferred alignment of the long axes of pores by bending of clay perpendicular to applied vertical stress.

Table 1: Core description, bulk mineralogy (McNeill et al., 2017b) and clay composition (Rosenberger et al., 2020) of the analysed samples. Bulk measurements were done shipboard on Expedition 362 (McNeil et al., 2017a; Underwood, 2020). Additional clay mineralogical analysis was done on the <2μm particle fraction onshore using a different instrument and methodology (Rosenberger et al., 2020). Here, Plag= Plagioclase feldspar, Smec= Smectite*, Chl= Chlorite, Kaol= kaolinite, Calc= Calcite.

	Sample no	Site	Hole	Core	Type	Sec	Depth	Unit	Bulk mineralogical comp (XRD)				Clay mineralogical comp (XRD)			
									Total clay	Quartz	Plag.	Calc.	Smec*	Illite	Chl+Kaol	Quartz
First set of sample (Analysed at Aachen university)	SN-1	U1480	E	1	H	1	1.24	I	68	12	9	11	25	58	68	12
	SN-2	U1480	E	1	H	4	5.10	I	67	12	9	12	24	60	67	12
	SN-3	U1480	E	2	H	1	9.18	I	71	15	12	2	38	49	71	15
	SN-4	U1480	E	2	H	2	10.69	I	66	15	10	9	36	59	66	15
	SN-5	U1480	E	3	H	6	26.05	I	62	19	11	8	40	43	62	19
	SN-6	U1480	E	4	H	1	28.00	IIA	63	21	13	3	14	62	63	21
	SN-7	U1480	E	9	H	2	63.24	IIA	64	20	13	3	11	67	64	20
	SN-8	U1480	E	10	H	2	74.07	IIA	65	20	12	3	21	58	65	20
	SN-9	U1480	E	11	H	5	87.98	IIA	60	21	17	2	6	74	60	21
	SN-10	U1480	F	2	H	1	98.25	IIA	63	19	16	2	7	77	63	19
	SN-11	U1480	F	3	H	3	111.10	IIA	67	17	14	2	6	76	67	17
	SN-12	U1480	F	15	F	2	176.50	IIA	62	22	14	2	13	69	62	22
	SN-13	U1480	F	26	F	1	226.70	IIA	70	17	11	2	22	58	70	17
	SN-14	U1480	F	53	X	2	369.19	IIB	68	18	12	2	21	53	68	18
	SN-15	U1480	F	59	X	1	426.68	IIB	68	18	11	3	9	69	68	18
	SN-16	U1480	F	67	X	CC	505.32	IIB	70	17	11	1	30	49	70	17
	SN-17	U1480	F	76	X	1	592.42	IIB	61	24	12	3	22	56	61	24
	SN-18	U1480	F	80	X	CC	630.55	IIB	68	15	14	2	19	59	68	15
	SN-19	U1480	F	91	X	1	737.39	IIB	67	19	12	1	36	46	67	19
	SN-20	U1480	F	92	X	1	751.16	IIB	67	19	12	2	36	46	67	19
	SN-21	U1480	G	4	R	2	776.17	IIB	70	18	12	0	40	39	70	18
	SN-22	U1480	G	7	R	CC	802.55	IIC	62	23	14	2	23	54	62	23
	SN-23	U1480	G	14	R	2	871.87	IIC	66	21	12	2	28	50	66	21
	SN-24	U1480	G	20	R	1	929.81	IIC	67	19	11	3	21	57	67	19
	SN-25	U1480	G	24	R	3	971.26	IIC	66	19	13	1	41	40	66	19
	SN-26	U1480	G	30	R	2	1027.91	IIC	65	22	13	0	21	51	65	22
	SN-27	U1480	G	37	R	2	1095.74	IIC	68	19	12	1	30	51	68	19
	SN-28	U1480	G	41	R	1	1119.70	IIC	69	16	12	3	19	57	69	16
	SN-29	U1480	G	45	R	1	1172.88	IIC	63	21	11	5	22	54	63	21
	SN-30	U1480	G	46	R	3	1184.39	IIC	65	17	12	6	18	57	65	17
	SN-31	U1480	G	51	R	CC	1233.15	IIC	61	23	12	4	17	59	61	23
	SN-32	U1480	G	55	R	6	1267.14	IIIA	68	19	12	1	64	25	68	19
	SN-33	U1480	G	59	R	1	1299.31	IIIA	72	15	12	0	54	36	72	15
Second set of sample (Analysed at BEG)	SN-34	U1480	H	2	H	2	6.25	IB	71	18	11	0	25	54	19	2
	SN-35	U1480	E	1	H	6	7.21	IB	70	12	10	8	24	55	19	2
	SN-36	U1480	H	3	H	1	14.28	IB	62	21	14	3	5	70	9	15
	SN-37	U1480	E	4	H	1	28.12	IIA	63	21	13	2	14	62	11	14
	SN-38	U1480	E	7	H	1	50.82	IIA	61	22	14	3	11	67	15	7
	SN-39	U1480	H	10	H	2	83.02	IIA	59	21	15	4	6	74	10	10
	SN-40	U1480	H	16	H	1	117.13	IIA	62	20	16	2	12	73	11	5
	SN-41	U1480	E	12	H	2	92.82	IIA	59	23	16	2	6	72	9	13
	SN-42	U1480	F	16	F	3	182.62	IIA	64	21	13	2	14	63	16	7
	SN-43	U1480	F	37	X	2	285.51	IIA	66	20	12	2	15	62	19	4
	SN-44	U1480	F	55	X	5	394.01	IIB	58	28	13	0	40	38	13	9
	SN-45	U1480	F	65	X	CC	486.72	IIB	59	26	14	1	30	49	14	7
	SN-46	U1480	F	79	X	1	621.2	IIB	66	19	13	2	19	59	19	4
	SN-47	U1480	F	91	X	1	737.47	IIB	67	19	12	1	36	46	14	4
	SN-48	U1480	G	11	R	1	841.56	IIC	63	22	13	2	26	51	19	4
	SN-49	U1480	G	23	R	1	959.15	IIC	58	26	14	2	33	46	18	3
	SN-50	U1480	G	30	R	1	1026.34	IIC	68	18	12	2	21	51	24	3
	SN-51	U1480	G	42	R	3	1145.91	IIC	60	22	12	5	14	61	18	7
	SN-52	U1480	G	54	R	2	1251.5	IIIA	63	22	13	1	16	53	16	16
	SN-53	U1481	A	23	R	5	1358.9	IIC	68	17	11	3	18	58	20	4
	SN-54	U1481	A	32	R	1	1432.5	IIIA	65	23	11	1	32	46	17	5
	SN-55	U1481	A	38	R	3	1493.3	IIIA	60	26	13	1	20	42	14	24

*Smectite includes all mixed-layer I/S; expandability of mixed-layer I/S determined separately (Rosenberger et al., 2020).